STUDY ON RESPONSE OF FORESTED CATCHMENTS TO CHANGING ATMOSPHERIC ENVIRONMENT IN THE FAR EAST OF RUSSIA

ZHIGACHEVA Ekaterina

(F19N502F)

Doctoral Program of Environmental Science and Technology

Graduate School of Science and Technology

Niigata University, Japan

Table of Contents

Abstract

Acid deposition and following acidification are processes that can be associated with the atmospheric pollution. Even with decreased emission levels of SO_2 and NO_X, acid deposition continues to be one of the important ecological problems in the world. A number of studies related to the ecosystem recovery from excess sulfur (S) and nitrogen (N) deposition have been published in different regions of the world. Even so, ongoing acidification could be found in some areas.

One of such examples is Komarovka river (KMR) situated in the Russian Far East. One of the sites for the Acid Deposition Monitoring Network in East Asia (EANET), Primorskaya, is situated there, providing a long-term data on wet deposition (WD), air concentrations for dry deposition (DD), and stream water (SW). However, the processes undergoing at the catchment are still not well understood. For the present study, the following objectives were defined: to evaluate the acidification situation and determine possible influencing factors of changing deposition and discharge fluxes; to compare the seasonal deposition and discharge trends at KMR; and to characterize the catchment in terms of sensitivity to atmospheric deposition in comparison to other sites in the Sea of Japan region.

Compared to the many other sites in the East Asia region, the climate at KMR is drier and colder during the winter. The ratio of sea-salt fraction in precipitation is quite low. At the same time, SW can be characterized by high alkalinity and buffering capacity. The upstream of the river belongs to the national reserve territories, and the influence of the human activities at the catchment itself is very low. Due to its whereabouts near the borders, KMR is a possible object of a long-range transport influence. Therefore, KMR can serve as a rather unique and interesting subject of study, based on which it could be possible to understand the acidification processes more precisely. In the study, the trend analysis of WD, DD, and SW fluxes was performed based on data from EANET monitoring.

Results for the period 2005-2020 are presented in this thesis. The DD fluxes were calculated from meteorological and air concentration data by the inferential method. The contribution of S by the DD flux into the total deposition was

decreasing from 2011 to 2018. The WD fluxes of sulfate (SO_4^{2-}) and nitrate (NO_3^-) have a changing point from decreasing to increasing after 2011 and 2014, respectively. Those trends seem to be not consistent with the latest trends of emissions that decrease in the region. Amount of precipitation tended to rise during the warm season starting around 2010, suggesting its contribution to an increase in fluxes of SO_4^{2-} and NO_3^-.

Phenomena of SW acidification was detected for KMR alongside with the increase of SO_4^{2-} and NO_3^- concentrations. In general, decreasing trend of pH in SW is going against increasing trend of rainwater pH. On the other hand, the recent increase in SW fluxes of SO_4^{2-} and NO_3^- could be attributed to the rise of precipitation amount during the warm season, following an increase in WD, and to the overall increase in SW discharge. The input-output balance shows discrepancies in S and Ca outputs, while uncertainties in flux estimations should also be taken into account. It was suggested that the excess S output could be attributed to the mobilization of S formerly accumulated on the catchment, including geological S weathering.

To better understand mechanisms of the acidification phenomena at KMR, the comparison with two sites of the same Sea of Japan region (Ijira and Kajikawa) was performed. These forested catchments were characterized by the higher levels of dissolved inorganic nitrogen (DIN) concentration in WD. However, NO_3^- concentrations in SW of KMR appeared to rise more significantly in response to deposition.

The study showed the phenomena of acidification of KMR SW in conditions of decreasing emission levels of acidifying precursors. The excess discharge of S suggests the possibility of mobilization of previously accumulated material into the SW. Also, the relationship between increases in deposition and discharge fluxes and the climate change was suggested. In addition, KMR appears to be more sensitive to the acidification compared to the sites of the same region. Thus, responses of forested catchments not only to changing atmospheric environment but also to the climate change should be further investigated in the future research.

List of Abbreviations

a.s.l.	above sea level
DD	Dry deposition
DIN	Dissolved inorganic nitrogen
EANET	The Acid Deposition Monitoring Network in East Asia
I-R method	Interval-Representative method
IJR	Ijira
ILC	Inter laboratory comparison
KJK	Kajikawa
KMR	Komarovka river
L-Q method	Load quantity of Flow method
nss-	Non-sea-salt
PCEM	Primorsky Center for Environmental Monitoring
ss-	Sea-salt
SW	Stream water
WD	Wet deposition

List of Figures

List of Tables

Chapter 1. Introduction

1.1 Acid Deposition

One of the problems appearing in result of air pollution is an acid deposition. Acid deposition is the process when acidic compounds/components (e.g., sulfuric acid, nitric acid and/or organic acids) are transported/deposited from atmosphere into the terrestrial and aquatic ecosystems (to the Earth's surface) in form of wet (rain, snow, cloud, fog) or dry (dry particles, gas) deposition. Entering the ecosystem, those compounds can acidify soil and surface waters and bring about a series of ecological changes (Driscoll et al., 2007).

Normally, not-polluted precipitation already has slightly acidic pH (5.0-5.5), but when pH values are decreasing below that level, they are considered acidified. The main chemical precursors for acids in the atmosphere are sulfur dioxide (SO_2) and nitrogen oxides (NOx). When these two compounds react with water, oxygen, carbon dioxide, and sunlight in the atmosphere, the result is sulfuric (H_2SO_4) and nitric acids (HNO_3) (Ramadan, 2004).

The largest source of anthropogenic SO_2 emission are combustion of fossil fuels, for electric generations and industrial processes. The main natural sources are volcanoes. Emission sources of NO_X are presented by fossil fuel combustion, biomass burning, and microbiological emissions from soils (Bouwman et al., 2002). The sources of nitrogen (N) in the form of NH_3 are animal wastes, fertilizers, biomass burning, loses from oceans and soils under natural vegetation, and industrial processes (Bouwman et al., 2002).

The gas-phase oxidation of both SO_2 and NO_2 is initiated by a reaction with hydroxyl radicals. The currently accepted mechanism of atmospheric SO_2 oxidation can be presented as (Berndt et al., 2008; Finlayson-Pitts & Pitts, 2000):

$$OH + SO_2 \rightarrow HSO_3 \quad (1)$$

$$HSO_3 + O_2 \rightarrow SO_3 + HO_2 \quad (2)$$

$$SO_3 + 2H_2O \rightarrow H_2SO_4 + H_2O \quad (3)$$

Reaction of NO_2 to the HNO_3 can be presented as follows (Finlayson-Pitts & Pitts, 2000):

$$OH + NO_2 \rightarrow HNO_3 \text{ (4)}$$

In equations 1-4, OH, HO_2, and HSO_3 are radicals.

Oxidation processes and following deposition of acids can occur both at relatively short distances from the emission sources and at distances of a 1000 km or more from.

Anthropogenic emissions of acidifying agents have started to increase in Europe and North America since the industrial revolution and peaked in 1970–1980 (Schöpp et al., 2003). Acidic deposition was first reported in the United Kingdom in the latter half of the nineteenth century (Gorham, 1992). The first ecological effects of acid deposition were documented in Scandinavia in the 1960s, related to surface water acidification and loss of fisheries (Gorham, 1992).

Among effects of acid deposition on catchment ecosystems, a decrease in pH and acid-neutralizing capacity (ANC) and alkalinity and an increase in base cation and aluminum concentrations are thought to be the most important. Those changes can lead to the accelerate soil weathering and nutrient removal as well as toxic elements mobilization (Ramadan, 2004). Soil acidification causes leaching of K^+, Ca^{2+} and Mg^{2+} and slowing down of phosphorous cycling (Carriera et al., 1997), decreasing the availability of these nutrients for vegetation. When N input is excessive, the increase in N availability may disturb the nutrient balance of plants because N is supposed to be the growth-limiting factor in many terrestrial ecosystems (Rennenberg & Gessler, 2001). Depending on the buffer capacity of the soil, extensive acid deposition increases the release and mobilization of Al from soil colloids. Together with high proton concentrations, dissolved Al inhibits the uptake of cations by plant roots (Rennenberg & Gessler, 2001). Under the influence of acidification, forests are becoming more vulnerable to the stress factors like climate anomalies and can lose their vitality (Bouwman 2002). The species diversity and abundance of aquatic life of stream water (SW) are also becoming endangered (Driscoll 2005).

The Convention on Long-range Transboundary Air Pollution (CLRTAP) signed in 1979 followed by implementation of emission-reducing policies, concentrations of air pollutant have reduced significantly. Since the adoption of CLRTAP, SO_2 emissions in Europe have decreased by over 80% (Duan et al., 2011; Evans et al., 2001; Grennfelt et al., 2020; Stoddard et al., 1999). Lately, processes of ecosystems recovery from acidification have become the new focus of research interest (Houle et al., 2010; Mitchell et al., 2013; Stoddard et al., 1999).

However, compared to the fast reduction in SO_2 emissions and the following decrease of S in soil solution and inland water (Johnson et al., 2018; Vuorenmaa et al., 2017), decrease in N emissions started only from 1990s (Engardt et al., 2017; Schmitz et al., 2019) was not so active. Thus, the problem of N leaching is still present (Schmitz et al., 2019).

1.2 Acid Deposition in East Asia

Compared to North America and Europe, the problem of Acid Deposition in Asia was detected later (Bhatti et al., 1992; Duan et al., 2016). In Japan and China, acidification of inland water in the 1990s has been reported in high-deposition areas and acid-sensitive areas (Duan et al., 2011; Matsubara et al., 2009; Nakahara et al., 2010; Yamada et al., 2007).

The reason in the delay could be the influence of high alkalinity of precipitation and acid buffering capacity of soils (Baba & Okazaki, 1998; Duan et al., 2016; Ohte et al., 2001; Suzuki, 2003). The differences in climate and vegetation are also one of the reasons.

Like that, the biogeochemical cycles of N and S highly depend on climatic conditions. As an example, climatic anomalies caused the acidification and N saturation in a forested catchment in central Japan (Nakahara et al., 2010). Climate change could also play a role in the processes of SW acidification. An increase in precipitation may increase the amount of SO_4^{2-} mobilized from internal sources (Mitchell et al., 2013; Mitchell & Likens, 2011; Sase et al., 2019; Shao et al., 2021). In the seasonal forest Thailand, changes in precipitation patterns influenced the

material discharge from ecosystems (Sase et al., 2017). The monsoon climate in Asia and seasonal precipitation patterns strongly influence the deposition processes of atmospheric pollutants (e.g. Sase et al., 2012). Changes in precipitation patterns and the frequency of extreme meteorological events have been recently reported in countries neighboring the Russian Far East, including Japan (e.g. Kawase et al., 2020; Shimpo et al., 2019).

Simultaneously, there is a possibility that acidification and/or NO_3^- leaching by excess N deposition has more significance for Asia. The leaching threshold in Asia is estimated to be 5 kg ha^{-1} yr^{-1}, which is significantly lower compared to the 10 kg ha^{-1} yr^{-1} for Europe and North America (Duan et al., 2016; Fang et al., 2011). Suspectedly, the effects by excess N deposition will have even bigger importance in the future.

Emissions of S and N have been decreasing in recent years in the East Asia region. For example, emissions of SO_2 and NO_X tend to be decreasing, starting the mid-2000s and in the early-2010s (Kurokawa & Ohara, 2020). Which is also later compared to the Europe and North America.

Air pollution monitoring in the East Asia started in 2001 under the Acid Deposition Monitoring Network in East Asia (EANET) with participation of 13 countries. Monitoring executed for four different media - wet deposition (WD), dry deposition (DD), soil and vegetation, and inland aquatic environment. Under the program, concentrations and fluxes of acidic substances deposited on the ground are measured and adverse impacts on terrestrial and aquatic ecosystems are estimated (www.eanet.asia).

Even if emission decrease started in Asia, the high levels of acidic compounds deposition still can be monitored for some regions (Figure 1.1). The Sea of Japan vicinity in 2020 had comparably low deposition levels for all the presented compounds (nss-SO_4^{2-}, NO_3^-, NH_4^+, and nss-Ca^{2+}). For some sites we also can see an increasing trends in pH of precipitation (EANET 2021). However, as for some regions acid deposition problem is still present, the primary goal of the EANET is still to understand the state of the acid deposition problems in East Asia and to

provide inputs for reducing adverse impacts on the environment. The processes of recovery are yet to be observed in the East Asian monitoring sites.

European part of the Russia is taking part in the European Monitoring and Evaluation Programme (EMEP) of CLRTAP. Meanwhile, territories in the Northeast Asia are monitored under the EANET. One of the four Russian EANET monitoring sites, Primorskaya, situated at the Komarovka river (KMR) catchment, was chosen as the main focus of this study. It has been used to monitor WD, DD, soil, vegetation, and inland aquatic environments since 2002.

Since 2009, there has been a significant decrease in pH and alkalinity and an increase in NO_3^- and SO_4^{2-} in SW of the KMR, (EANET, 2016a, 2016b). During the same period (2010-2014), the acidity of the WD at the Primorskaya site decreased, while the ratio of acid anions relative to base cations in rainwater increased (EANET, 2016b). In 2020, mean annual WD pH reached 6.0, which is the highest value for the site during the monitoring history (EANET, 2021). Difference in trends, presented in EANET reports calls attention to origins of that phenomena which lead to the present study.

1.3 Objectives

The objectives of the present PhD study were:

- to evaluate the acidification situation in SW of KMR (EANET site Primorskaya),
- to determine possible influence of changing deposition levels and other environmental factors on SW of KMR, and to estimate whether those changes could be a possible mechanism of SW acidification phenomena,
- to estimate trends in seasonal data series for KMR,
- to compare the seasonal trends in deposition and discharge fluxes,
- to characterize the study forested catchment in terms of the sensitivity to atmospheric deposition compared to neighboring sites in the Sea of Japan region.

For assessments, a SW chemistry and atmospheric deposition data for the last 16 years (from 2005 to 2020) was used in this study.

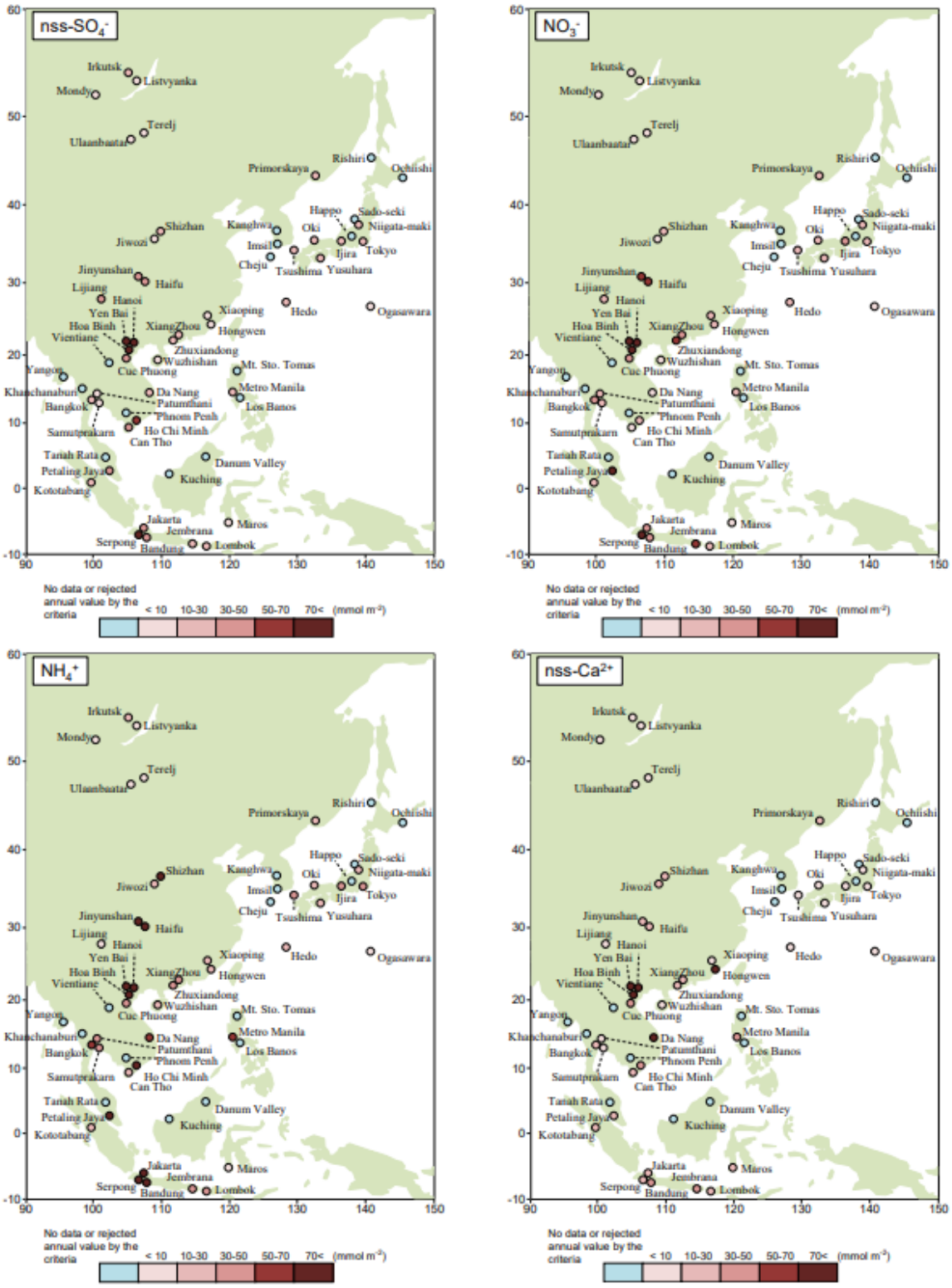

Figure. 1.1 Annual WD levels of nss-SO_4^{2-}, NO_3^-, NH_4^+ and nss-Ca^{2+} in 2020 (from (EANET, 2021).

Chapter 2. Komarovka – Primorskaya site

2.1 Importance of the Komarovka river

The KMR catchment is situated in Far East Russia (43° 42′ N 132° 07′ E, Figure 2.1) and belongs to the Primorsky Krai of Far Eastern Federal District of Russia. Primorsky Kray face the western coasts of the Sea of Japan. It shares borders with China in the west and North Korea in the southwest.

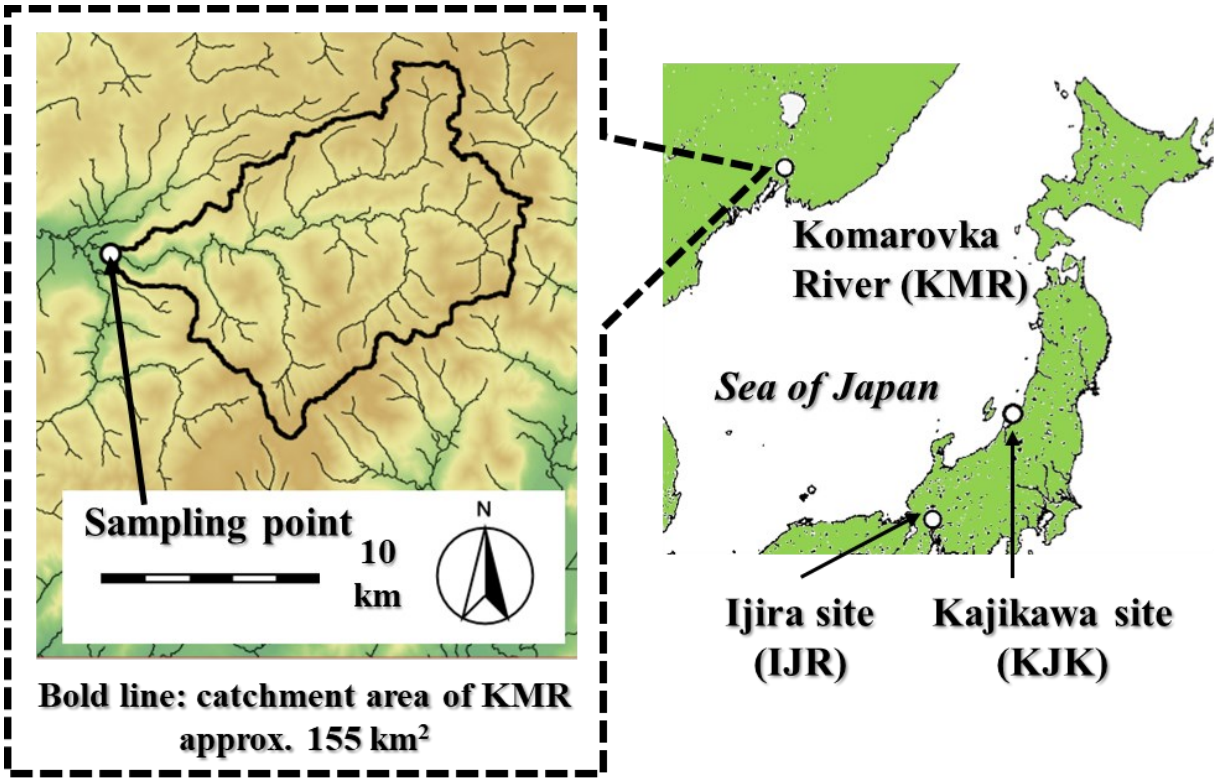

Figure 2.1. The map of the KMR catchment area (right) and the location of Vladivostok City, Ussuriysk City, and other reference monitoring sites in Japan, Kajikawa (KJK) and Ijira (IJR) (left) (from Zhigacheva et al. 2022) .

The two biggest cities in the vicinity are Ussuriysk (population: approximately 173 thousand) located 25 km northwest and Vladivostok city (population: approximately 600–606.5 thousands for 2013–2020) located 60 km south–southwest of the river catchment. The sampling point at KMR is located approximately 35 km north from the seacoast.

There are still not so many works related to acid deposition monitoring and influence for the Russian Far East region. It is not a well-studied region. And for KMR monitoring of deposition and SW chemistry started at the beginning of 2000s,

making it possible to estimate long-term effects. According to the EANET reports, the acidification of SW of KMR is continues although deposition levels of monitoring compounds are low.

Almost no influence of human activity can be found at the catchment. The upstream of KMR is situated at the Ussuriysky Nature Reserve territories. Thus, it can be thought as a territory of quasi-natural state with background pollution levels. At the same time, KMR, which is situated near the borders of China and Korea, can be influenced by the transboundary air pollution. The SW of KMR is characterized by high alkalinity and buffering capacity. But the climate is quite different compared to the other sites of the Sea of Japan region.

Additionally, the Primorskaya EANET deposition-monitoring site (meteorological station) is located adjacent to the KMR sampling point and functioning starting 2002, making a long-term data assessment available.

All aforementioned conditions make KMR an interesting model object for studying the influence of atmospheric deposition on the chemistry of surface waters in the Primorsky region.

2.2 Site description

KMR is a mountain river which originates in spurs of the Sikhote-Alin Ridge is a left tributary of Razdolnaya River flowing into the Amur Bay in the Sea of Japan. The catchment area until the sampling point is estimated to be around 155 km^2 (Figure 2.1). The highest elevation is 680 m a.s.l. The Primorskaya meteorological station and SW sampling point for KMR are located 85 m above sea level (a.s.l.) presenting the lowest point of the studied area (Figure 2.2).

The Primorskaya EANET Deposition monitoring site was established in 2002 within the meteorological station and was classified as a rural site. Hydrochemical observations on the site started since 2005. The meteorological data used in this study were measured at the meteorological station. A hydrological post Tsentralny where water regime data are monitored is situated a little bit further downstream.

Figure 2.2. Sampling points for meteorological data, precipitation, and air (left), and river water (right)

The annual precipitation is 782.0 mm, and the annual mean temperature is 4.2 °C. The lowest and highest temperatures are −16.3 °C in January, and 21.0 °C in August, respectively (Figure 2.3, left). The lowest monthly mean temperature during the monitoring period 2005-2020 was −20.5 °C in January 2012, and the highest was 22.4 °C in August 2010.

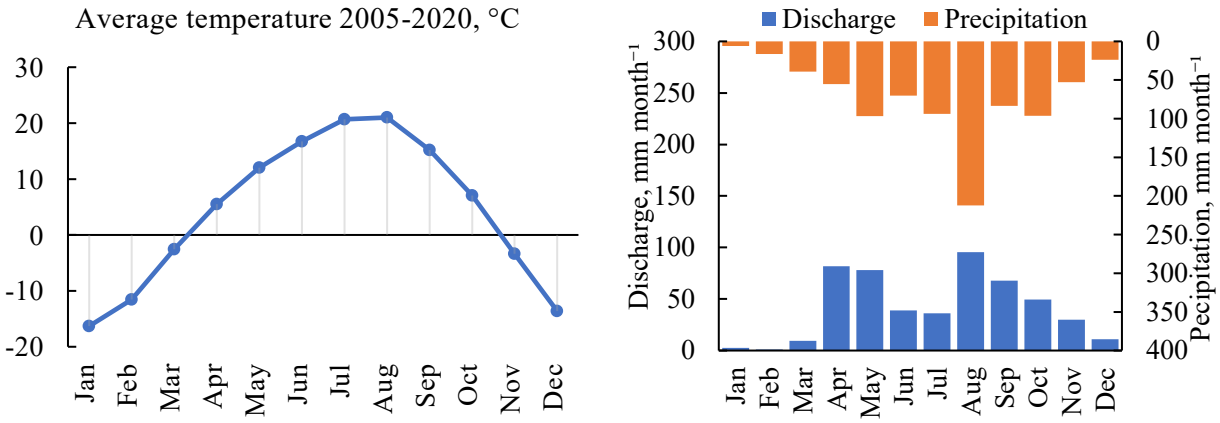

Figure 2.3. Seasonal changes in monthly average temperature (left), monthly average precipitation and monthly average discharge of SW (right). Averages for precipitation and SW discharge are calculated for 2005, 2010, 2012, 2015, 2018, 2019, 2020. (Updated from Zhigacheva et al. 2022)

Mean annual river water discharge according to the data from the hydrological station "Tsentralny" varies from 300.0 mm to 599.6 mm. The mean runoff rate based on available daily discharge data is approximately 56%. The mean runoff rate from June to September is approximately 55%, which is within the range of the seasonal values observed in the region (Lupakov, 2021). The water temperature measured

alongside the sampling in the river changed from 0.1°C (on February and November) to 20.1°C (In July).

The pattern of SW discharge is closely related to rainfall, with peak discharge and precipitation in August (Figure 2.3). Annual water runoff discharges correlate well with the annual precipitation (r = 0.85). Level of precipitation during the winter is extremely low. Alongside with the temperatures below 0 °C it leads to the low or almost no water discharge as the SW is mostly frozen. The snow-melting season at KMR starts in April and ends in May (Bogatov et al., 2013). Although precipitation level at that time is still not so high, the peak of SW discharge can be observed.

The catchment is fully covered by broadleaved forests with *Pinus koraiensis*, except for the open areas of the meteorological station and service corridors. The main tree species present are *Quercus mongolica* Fisch. Ex Ledeb, *Acer mono* Maxim., *Tilia amurensis* Rupr., and *Fraxinus mandshurica* Rupr. Soils present in the catchment area are Umbric Cambisols and Mollic Liptosol according to the classification by the World Reference Base for Soil Resources (WRB) (EANET 2007; EANET 2014).

2.3 Emission sources in the region

KMR catchment is supposedly not influenced by local anthropogenic activities in the vicinity of its area. However, because this area is surrounded by other countries such as China, ones in the Korean Peninsula, and Japan, the atmospheric environment at the Primorskaya site may have been influenced by both transboundary transport of pollutants from neighboring countries and dispersion of pollutants emitted from industrial and large cities of Russian Far East region, such as Vladivostok.

As it was discussed in chapter 1, there are decreasing trends of SO_2 and NOx emissions in East Asia in the last decades. For the Far East of Russia, anthropogenic emissions have also been decreasing; from 2010 to 2019, SO_2 and NO_X decreased by 26.9% and 14.7%, respectively (Ministry of Natural Resources and Environment of the Russian Federation, 2020).

2.4 Estimation of air mass transport routes

Using the Hybrid Single-Particle Lagrangian Integrated Trajectory model (HYSPLIT), the main directions of compounds transport to the KMR catchment was estimated. For the calculation, Primorskaya site was chosen as the end point and the end time was established to be the same as the air sampling time. In total, there were 24 distribution maps were calculated for the 2018, Two of characteristic trajectory frequency maps are presented in Figure 2.4. All the 24 trajectory frequency maps are presented can be seen at appendix 1.

Conditions for calculation were:

- Endpoint coordinates: 43°37'44" N 132°14'17"E
- Trajectory frequencies calculation period: between the air sampling period (about 2 weeks – every 15th and last day of the month 12am UTC)
- Height of the airmass trajectories estimation: 500 m
- Length of every airmass trajectory: 72 hours

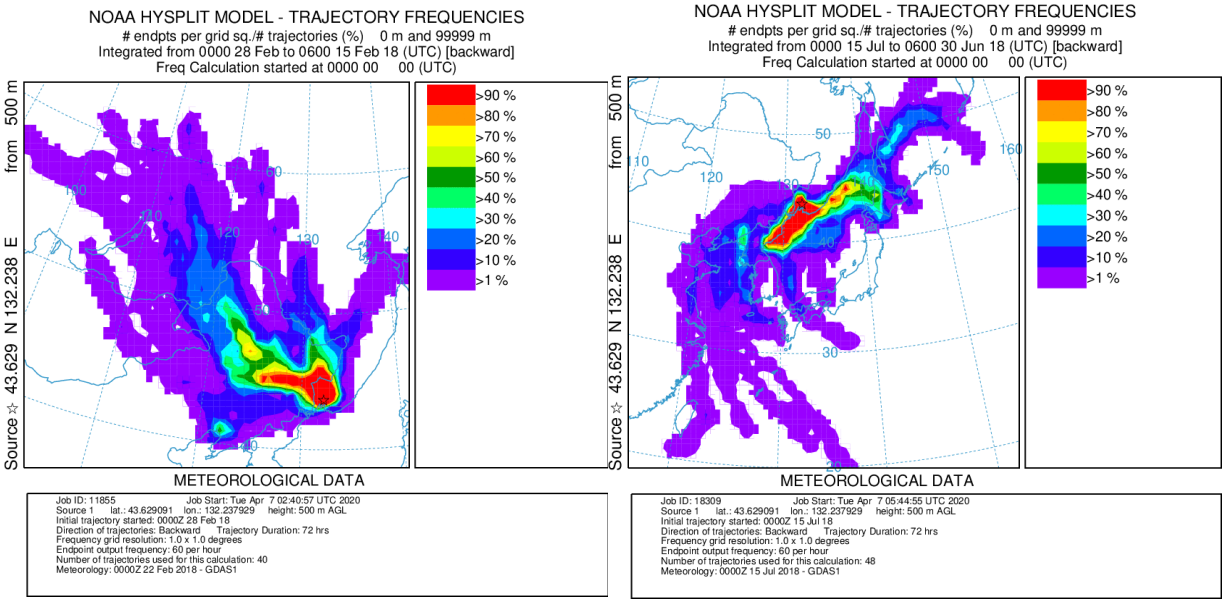

Figure 2.4. Distribution of trajectory frequencies consisting of 72-hours backward airmass trajectories arriving to the monitoring Primorskaya site. Left: for period from February 15 to February 28. Right: for period from June 30 to July 15.

It could be seen that during the winter season the majority of the airmass is coming from the North-West, arriving mostly from Western parts of Russia and

China. During the summer most of the air masses come from the Sea of Japan side. Yet only one year was estimated in relation to the air-mass movements, and conclusions about long-range transport of pollutants are preliminary.

At present moment only airmass movement directions and frequencies were estimated. But HYSPLIT in correlation with deposition estimation could be used for determining the main sources of pollutants deposited to the catchment. Like that, Inomata et al (2019), using S isotopic ratio and mass balance calculations, showed the air mass transport routes and precipitation pattern in Japan. The major part of the transboundary transported anthropogenic SO_4^{2-} is deposited at the Sea of Japan side of Japan with the highest amount of deposited S during the winter.

Chapter 3. Atmospheric Pollution Impact on Komarovka river catchment

3.1. Input (Total deposition flux)

3.1.1. Wet Deposition

3.1.1.1. Sampling and calculation methods

In the present study, the total deposition flux was calculated only using the WD and DD fluxes

$$Input = Wet\ deposition\ (WD) + Dry\ deposition\ (DD) \quad (5)$$

Samplings of atmospheric WD are presented as rain and snow. An automatic precipitation sampler is installed in the open area at the Primorskaya meteorological station (Figure 2.2 left). Collected 24-hour samples are gathered from sampler daily at 9 a.m. The samples collected in the field are stored in a refrigerator in the laboratory at the site and later are transported to the Primorsky Center for Environmental Monitoring (PCEM), Russian Federal Service for Hydrometeorology and Environmental Monitoring (Roshydromet), Vladivostok. At the PCEM chemical analysis of the samples is performed according to the techniques adopted in EANET (EANET, 2010a)

The analytical data for WD were assessed for ion balance and EC in the laboratory according to the EANET Technical Manuals (EANET, 2010a, 2010b). The data used in this study were checked at the national center of Russia before submission, verified by international experts of the respective study fields during data compilation at the NC, and then authorized by the Scientific Advisory Committee of EANET (Zhigacheva et al. 2022).

The PCEM laboratory also take part in inter-laboratory comparison (ILC) projects, performing analysis on artificial rainwater and inland water samples. Results of ILC are published annually by EANET and can be accessed through its site. Some outliers were found in recent years for WD (artificial rainwater) samples,

probably because some of analytical procedures, such as dilution of the ILC samples, were inconsistent with procedures for WD field samples (Zhigacheva et al. 2022).

The official EANET data is disclosed on the website (EANET, 2022). Data on monthly and annual fluxes can be downloaded from the EANET website (EANET, 2021). For the WD, the data on pH, electrical conductivity (EC), SO_4^{2-}, NO_3^-, Cl^-, NH_4^+, Ca^{2+}, Mg^{2+}, K^+, and Na^+ are available.

Data for the period 2005-2020 were accessed in the study. For calculations mainly MS Office Excel was used. According to the (EANET, 2021), calculations used for the WD are as follows:

$$\hat{C} = \Sigma (Ci Pi) / \Sigma Pi \quad (6)$$

where $\hat{C}$ - precipitation amount weighted average concentration (μmol L^{-1}), Ci - measured valid concentration for sample i (μmol L^{-1}), Pi - precipitation amount (mm) for the same sample i with valid concentration

The wet deposition amount ($mmol\ m^{-2}$) for the period calculated as:

$$Dep.amount = \hat{C} \times P/1000 \quad (7)$$

Where P - total precipitation amount (mm) for the summary period.

Means for pH were calculated through $[H^+]$ concentrations. Dissolved inorganic nitrogen (DIN) is calculated as a sum of NO_3^- and NH_4^+.

For statistical analysis (Mann-Kendall test, Spearman's rank correlation) - R with package 'trend' version 1.1.4 and package 'stats' version 4.0.3 was used.

3.1.1.2. Trends of wet deposition

Based on annual data of WD for period 2005-2020, the trends were calculated. The lowest mean annual pH value (4.63) was monitored in 2011. Since then, pH continues to increase, and the highest value appeared in 2020 (6.0). The Mann-Kendall test shows the statistically significant increase for the whole period ($p < 0.001$) (Table 3.1) The pH does not correlate with the changes in precipitation (Spearman's rank correlation, $p = 0.16$; Figure3.1 a).

Cl^- and Mg^{2+} have a statistically significant increasing trends ($p = 0.0344$ and $p = 0.0079$, respectively). Annual mean concentrations of other major ions in

rainwater did not show any significant trends. (Table 3.1, Figure 3.1 b-f).

Before 2011, SO_4^{2-} in WD were clearly decreasing, but after that a tendency for increase can be observed. The same situation can be observed for Ca^{2+}.

Table 3.1. Trend analysis using the Mann-Kendall test for WD for period 2005-2020

	Z score	p-value
SO_4^{2-}	-0.86	0.3923
NO_3^-	0.68	0.4995
Cl^-	2.12	0.0343
NH_4^+	-1.49	0.1373
Na^+	1.94	0.0529
K^+	1.85	0.0649
Ca^{2+}	0.05	0.9641
Mg^{2+}	2.66	0.0079
DIN	-0.86	0.3923
pH	3.47	0.0005
Precipitation	0.86	0.3923

3.1.1.3. Cation-Anion charge balance

Cation-Anion Charge balance was estimated for the whole period of 2005 – 2020 (Figure3.2 a, b), as well as for three 5-years periods (Figure 3.2 c). Ion balance between the sea-salt and non-sea-salt fractions is well balanced. While anion mEq amount is slightly underestimated compared to the cations they still stay comparably balanced.

As sea salt is not contributing to acidification of the deposition and for the studied area sea salt contribution is supposed, non-sea salt fractions of SO_4^{2-} and Ca^{2+} were estimated.

Both cations and anions are divided on two fractions: sea-salt fraction (ss-) and non-sea-salt fraction (nss-). Cl^-, Mg^{2+}, K^+ (assumed fully belong to ss-fraction) and Na^+ belong to the ss-fraction. NO_3^-, H^+, and NH_4^+ belong to the nss-fraction. SO_4^{2-} and Ca^{2+} can belong to both fractions and it is showed by prefixes.

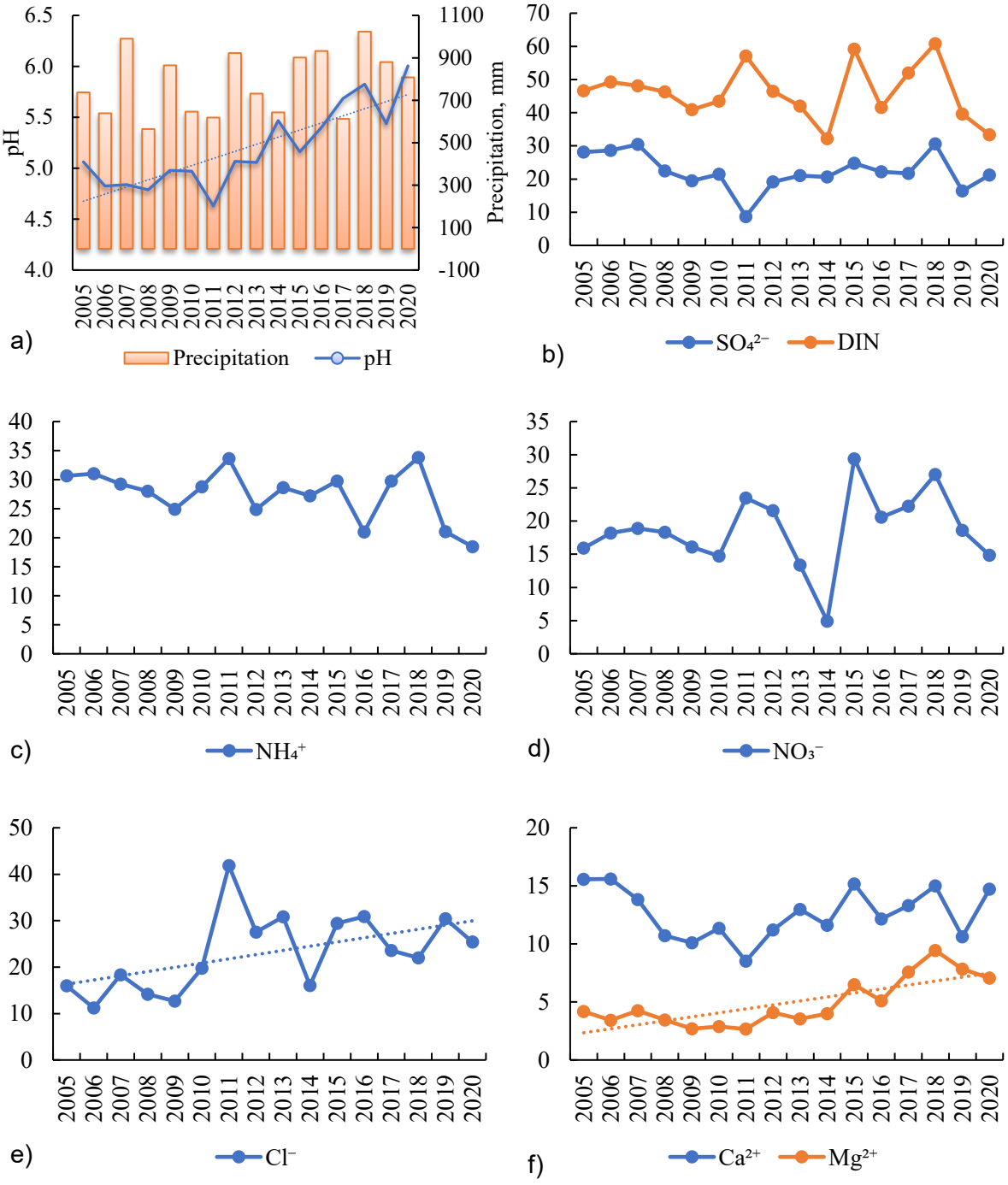

Figure 3.1. WD annual data on pH, Precipitation amounts (mm), and major ions: SO_4^{2-}, DIN, NO_3^-, NH_4^+, Ca^{2+}, Mg^{2+}, Cl^- (mmol m^{-2}). (Updated from Zhigacheva et al. 2022)

Division of sea salt and non-sea salt for SO_4^{2-} and Ca^{2+} is calculated based on the concentration of Na^+. It is accepted that sea-salt $(SO_4^{2-}/Na^+)_{mol}$ =0.060 or sea-salt $(Ca^{2+}/Na^+)_{mol}$ =0.022.

$$Sea\ salt\ concentration = Na^+(rainwater) \times (M/Na^+)\ sea \quad (8)$$

$$Non\ sea\ salt\ concentration = M(rainwater) - Sea\ salt\ concentration \quad (9)$$

where M is molar concentration of SO_4^{2-} or Ca^{2+}.

Contributions of sea-salt (ss) fractions, such as ss-SO_4^{2-} and ss-Ca^{2+}, to atmospheric fluxes are very low at the Primorskaya site (Figure 3.2). Although the Primorskaya site is situated inland but not far from the sea, due to the climate and geographical location the influence of marine atmospheric masses on deposition is limited. In general, nss-fraction accounts for more than 65% of WD. However, there is no direct correlation between the nss-SO_4^{2-} and pH (Spearman's rank correlation p = 0.98)

3.1.1.4. Seasonal trends

Based on meteorological conditions (Figure 2.3), two seasons could be distinguished for KMR catchment. Cold season from October to March is characterized with low temperatures (mostly below the 0°C) and low amount of precipitation. Warm season from April to September with mean temperatures higher than the 0°C when the most amount of precipitation is falling. The precipitation in the warm season was almost twice as much as that in the cold season, and this seasonal difference has increased in the last decade (Figure 3.3 a). The pH did not differ between seasons and tended to increase from 2012/2013, which cannot be attributed to change in analytical conditions. (Figure 3.3 b).

The WD fluxes of SO_4^{2-} and DIN for the cold and warm seasons are shown in Figure 3.3 c-d. NO_3^- and NH_4^+ separately as well as Ca^{2+} and Cl^- are shown in Figure 3.3 e-h.

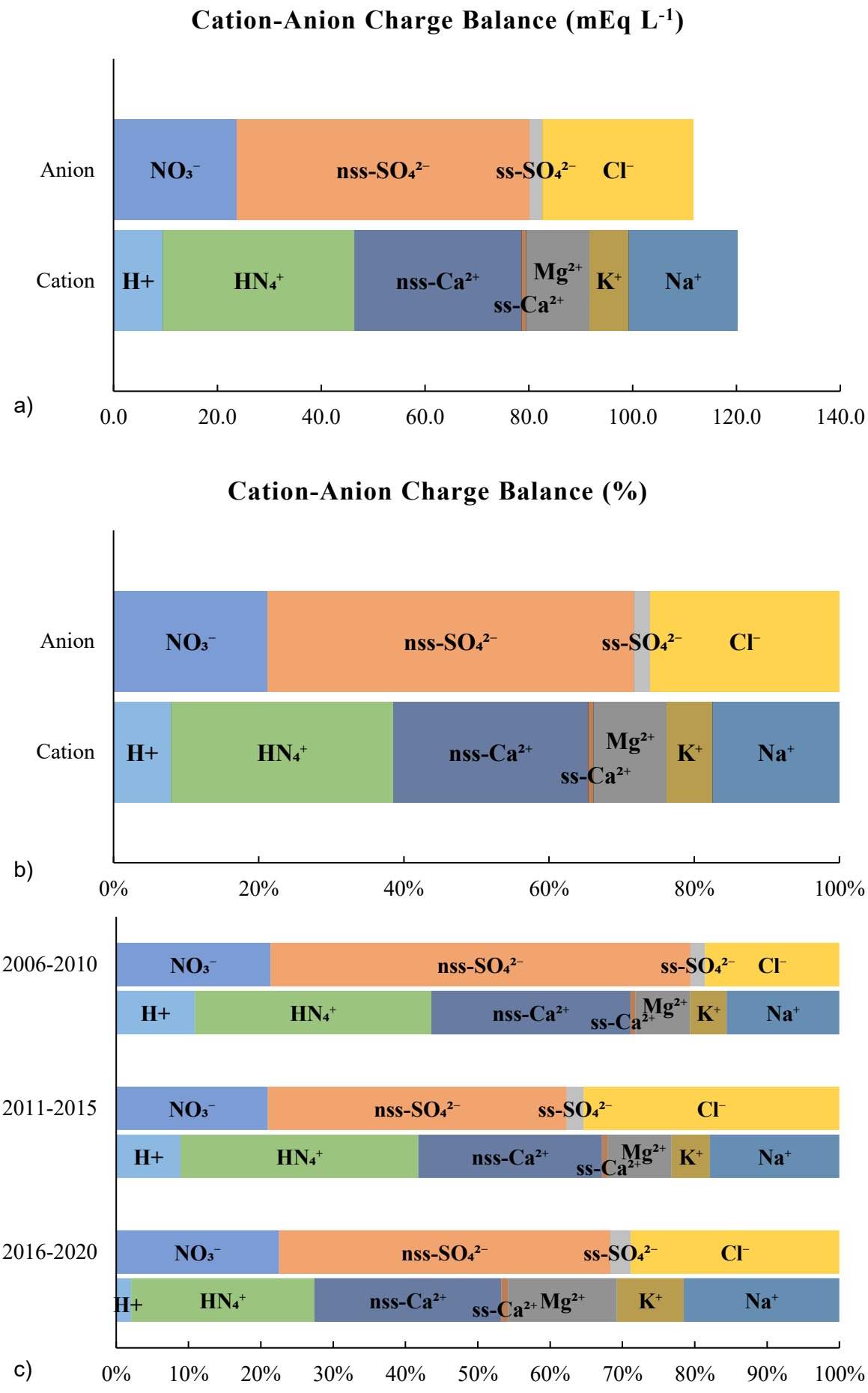

Figure 3.2. Cation-Anion Charge Balance by mEq L^{-1} and precent composition

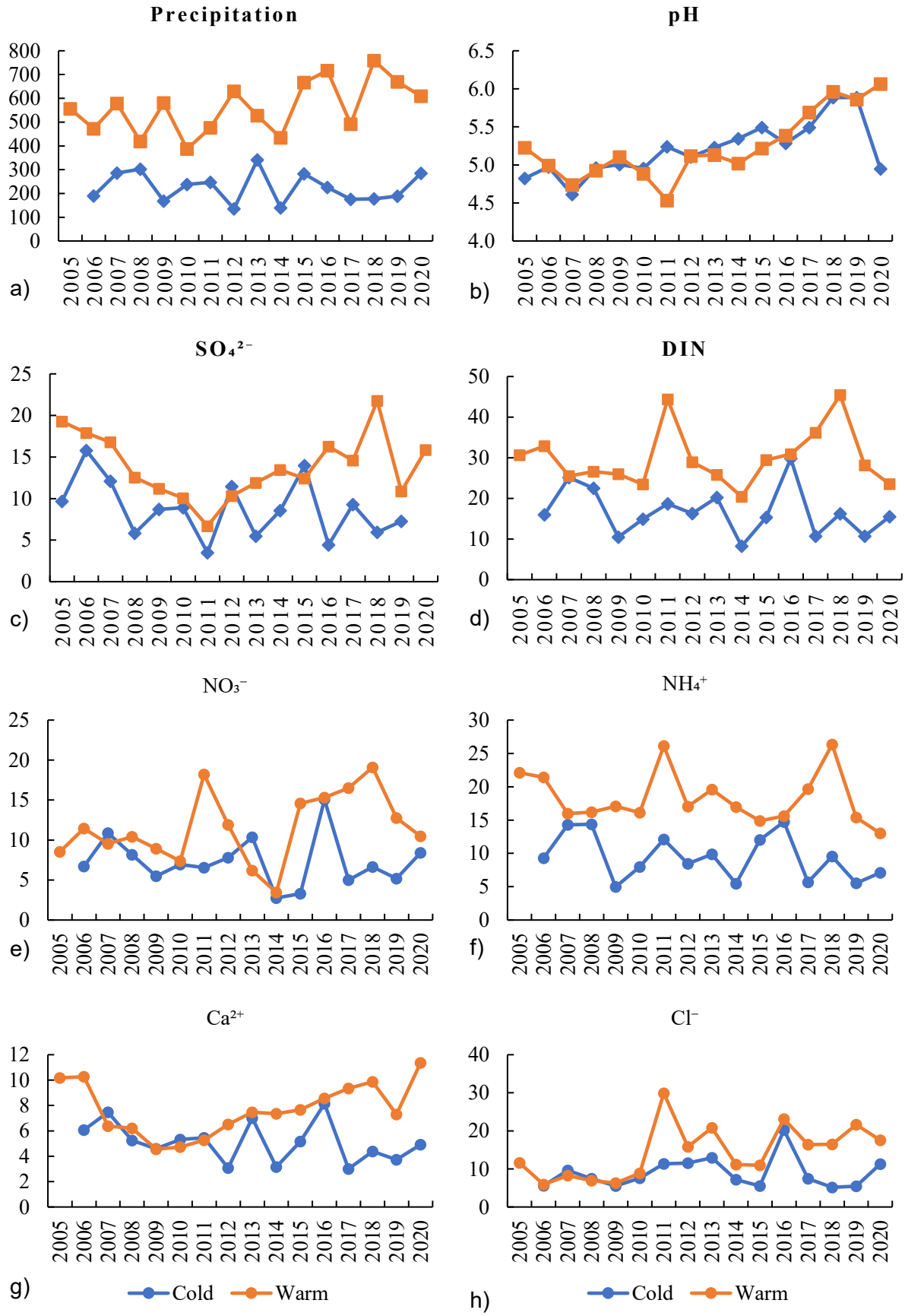

Figure 3.3 Interannual variations in the annual precipitation amounts, mean pH, and major ions WD (mmol m^{-2} $season^{-1}$) during the cold and warm seasons of 2005–2020 during the cold (October–March) and warm (April–September) seasons. (Updated from Zhigacheva et al. 2022)

Although concentrations in WD during the cold season were relatively high, the fluxes in the warm season were higher than those in the cold season due to much higher precipitation.

The SO_4^{2-} flux in the warm season showed a clear transition from a decreasing trend to an increasing trend in 2011. The DIN fluxes showed clear increased from 2014 to 2018 after the transition in 2014. Those transitions are more clearly visible compared to the annual WD trends. The fluxes for SO_4^{2-} and DIN tended to be slightly lower in the cold season than in the warm season. Ca^{2+} and Cl^- show an increase in the fluxes during the warm season starting from 2009 and 2010, respectively. Increasing precipitation during the warm season contributed to the WD fluxes increase. As a result, the difference in deposition fluxes between the seasons became larger.

3.1.2. Dry deposition

3.1.2.1. Sampling and calculation methods

The DD was estimated based on the air concentrations using the Filter Pack (FP) method and meteorological conditions according to the Technical Manual on Dry Deposition Flux Estimation in East Asia (EANET, 2010b).

By using it, the DD flux of gaseous and particulate species is calculated by the inferential method as the product of air concentration and respective deposition velocity (V_d):

$$F_i = V_{d_i} \times C_i \qquad (10)$$

where F is the flux of species *i*, and C is the concentration of species *i*. After hourly or daily deposition velocities are calculated, the deposition velocities are averaged in the time resolution of air concentration.

Data on gaseous substances (SO_2, HNO_3, HCl, NH_3) and particulate matter components (SO_4^{2-}, NO_3^-, Cl^-, NH_4^+, Ca^{2+}, Mg^{2+}, K^+, and Na^+) were calculated using the FP method (EANET 2013, 2021). Air samples are taken at Primorskaya site twice a month (continuously using a four-stage filter pack), meaning approximately

two-week samples are collected. Meteorological data, such as temperature, relative humidity, wind speed, solar radiation, precipitation, cloud coverage, were used to calculate V_d, as described below. The relevant meteorological data are taken at the Primorskaya meteorological station. Data on solar radiation acquired at the Timiryazevskii meteorological site near Ussuriysk (43°51' 25.6" N 131°57'10.7" E) - until 2017.

For calculation of V_d, Microsoft Excel macro program provided by EANET Network Center was used.

3.1.2.2. Calculation uncertainties

According to the requirement for the input data, values of every parameter should be input into the excel table for every hour of studying period. Among meteorological data needed (Temperature [˚C], Relative Humidity [%], Wind Speed [m s^{-1}], Solar radiation [MJ m^{-2}], Precipitation [mm], Cloud coverage [0~10]), only solar radiation values were available on hourly basis and other parameters are all on daily basis. Therefore, after the changes of processing format, the averaged parameter values ("Daily") were applied for the program performance.

Most of the territory of the KMR catchment is covered with forest trees, with negligible open areas. For calculations it was assumed that 100% of catchment covered by forests and calculations for open (grass type) areas were not carried out.

Data on vegetation was acquired from EANET Data Report 2006 (EANET. 2006). Values of land-use categories were used for V_d calculations as follows in Table 3.2.

Table 3.2 Values of land-use categories

Reference Height	40 m
WS (wind speed) Height	40 m
Canopy Height	30 m
Displacement Height	0.7 Canopy Height
Roughness Height	1.05 m (EANET. 2010)

Starting from 2018 data on solar radiation became unavailable, so for the last three years means of respective dates daily solar radiation data were used. As result, calculated values are used only for acquainting and statistical estimation for DD was not performed.

3.1.2.3. Total atmospheric fluxes

The atmospheric inputs are calculated as the sum of WD and DD. The total atmospheric S flux may include fluxes of SO_4^{2-} dissolved in rainwater as WD and gaseous SO_2 and particulate SO_4^{2-} as DD. The total flux of DIN includes fluxes of NO_3^- and NH_4^+ dissolved in rainwater as WD, gaseous HNO_3 and NH_3, and particulate NO_3^- and NH_4^+ as DD. The total Ca^{2+} flux may include fluxes of Ca^{2+} dissolved in rainwater as WD and particulate Ca^{2+} as DD. The total Cl^- flux may include fluxes of Cl^- dissolved in rainwater as WD and gaseous HCl and particulate Cl^- as DD. The atmospheric fluxes were expressed as mmol m^{-2} $year^{-1}$, or kmol km^{-2} $year^{-1}$. The changes in the annual total atmospheric fluxes by WD and DD are shown in Figure 3.4.

The WD flux played a larger role in the total flux. Contributions of DD fluxes to the total fluxes for S, NOx, and NHx were 33%, 33%, and 38%, respectively.

The total flux of S tended to decrease until 2011, and thereafter the trend became unclear (Figure 3.4 a), which mostly follows the WD trends. The WD flux of SO_4^{2-} increased from 2011 to 2018, lowering the contribution of the DD flux. The total flux of inorganic N decreased from 2011 to 2014, and thereafter turned to increase (Figure 3.4 b). The total flux of Ca^{2+} showed similar variations to that of S. For the total flux of Cl^-, the highest flux was observed in 2011 with increased contributions of DD (47.5%, the 3 years mean from 2010 to 2012). At the beginning of the observational period, the flux of Cl^- at the Primorskaya site was considerably low. The HCl concentration levels measured in the air were 0.1–0.2 ppb and 0.7–1.1 ppb in 2005–2009 and 2010–2012, respectively (EANET, 2020). The fluxes of Cl^- showed a clear peak in 2011 and then gradually decreased (Figure 3.4 d).

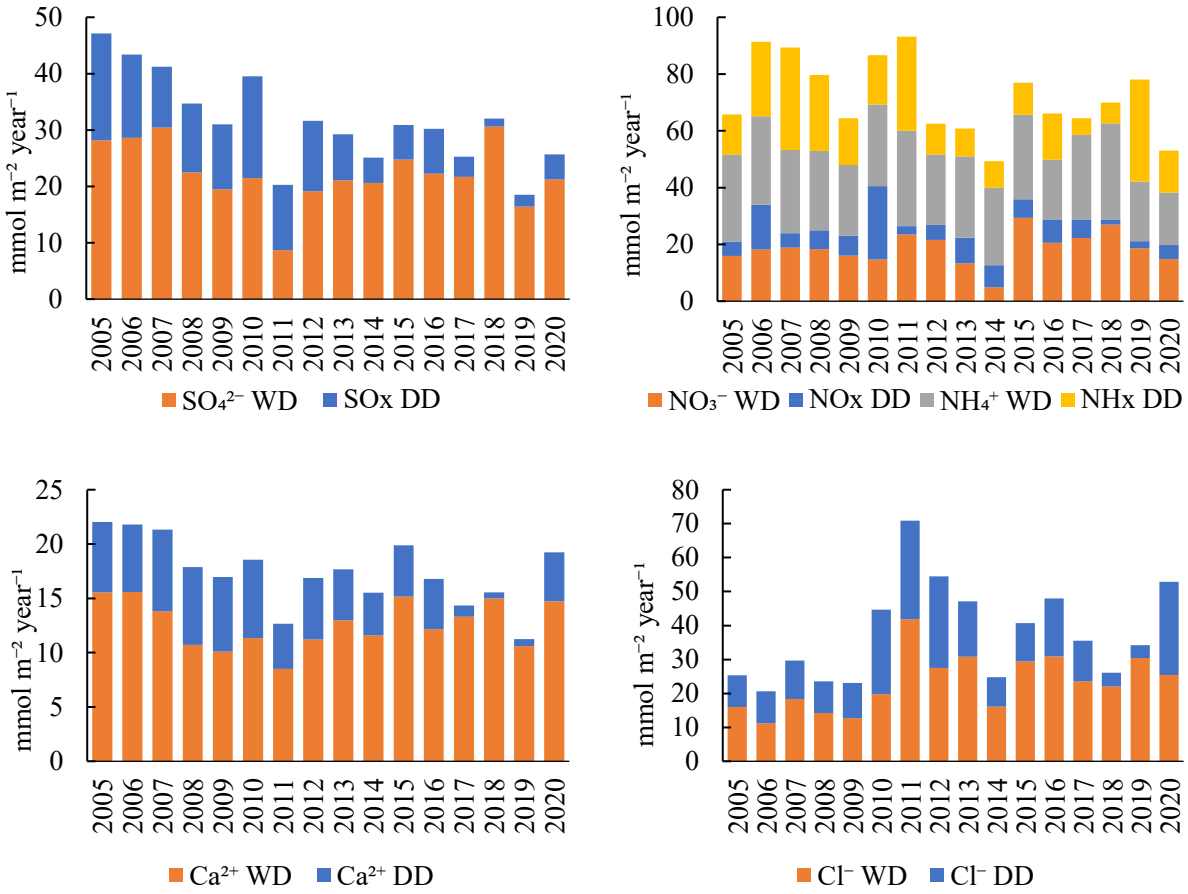

Figure 3.4 Total atmospheric fluxes by WD and DD for S (a), N (b), Ca (c), and Cl (d). WD, wet deposition; DD, dry deposition. (Updated from Zhigacheva et al. 2022)

Emissions of SO_2 and NOx peaked in 2006 and 2011, respectively (Kurokawa and Ohara 2020). For the Far East of Russia, anthropogenic emissions are also decreasing (Ministry of Natural Resources and Environment of the Russian Federation, 2020). It appears that trends of deposition fluxes did not follow the latest regional emission trends in East Asia. But the ground observational data on atmospheric deposition may not necessarily reflect the national emission trends estimated based on the statistics in the respective countries (Sase et al., 2021; Zhigacheva et al., 2022).

3.2. Output (Stream water discharge)

3.2.1. Sampling and calculation methods

SW samples of KMR are collected five times a year (since 2007 - in February, April, June, September, and November) in correspondence with the main hydrological regime periods. February is characterized by extremely low water

discharge levels. April is a snow melting period and the start of the spring flood. June and November are periods of the base flow. In September increasing discharge levels are monitored.

The SW flow rate (m s^{-1}) was measured together with the water sampling. Data on pH, electrical conductivity (EC), SO_4^{2-}, NO_3^-, Cl^-, NH_4^+, Ca^{2+}, Mg^{2+}, K^+, and Na^+, for SW data on alkalinity (by the endpoint-4.8 method) are available through the EANET. The analysis procedures, quality check procedures and statistical method can be found at the WD sampling (chapter 3.1.1). There were some outliers for the ILC projects for the artificial inland water samples for the laboratory, but in general the results are considered acceptable. In this study, the chemical data disclosed from the EANET website were used for the analysis, while the flow rate data were obtained from the Roshydromet.

As sampling is performed only five times per year, the calculations of annual fluxes may have several uncertainties. Thus, data on concentrations from every sampling was used for trend analysis using the Mann-Kendall test. Output with SW was calculated using two methods: the interval-representative (I-R) method and load quantity of flow (L-Q) method. The material fluxes as the output from the forested catchment were expressed as kmol km^{-2} $year^{-1}$.

For the I-R method, the flux was calculated directly as a product of concentration by water discharge for the days of sampling. The flux was calculated for the periods between sampling by multiplying the average measured concentrations of dissolved constituents in SW sampled at the beginning and end of an interval by the flow volume during a given period (Likens & Bormann, 1995; Sase et al., 2019).

3.2.2. L-Q method calculations

The L-Q method was used for the years in which daily data on water flow discharge were available (2010, 2012, 2015, 2018, 2019, and 2020). The daily data were acquired from the hydrological station “Tsentralny”, situated right downstream

the SW sampling point. For the L-Q method, we used the following regression equation for the calculations (Ide et al., 2007):

$$L = aQ^b \quad (11)$$

where L is the load, Q is the discharge, and a and b are empirical parameters, calculated using MS Excel regression exponential trendline estimation based on the available datasets of concentrations and water discharges for the respective ionic constituents.

Equation by which further daily compounds discharge flux is calculated presented in Table 3.3. Graphical results of regression estimation performed at MS Excel are presented in Appendix 2.

Table 3.3. Results of L-Q equation calculations

Ions	L=	R^2
SO_4^{2-}	$116.95x^{0.9745}$	0.8368
NO_3^-	$23.183x^{1.0211}$	0.4184
Cl^-	$91.97x^{0.9865}$	0.9569
NH_4^+	$7.2119x^{1.2156}$	0.6439
Na^+	$156.89x^{0.9824}$	0.9677
K^+	$18.632x^{1.0761}$	0.8260
Ca^{2+}	$212.98x^{0.9865}$	0.9782
Mg^{2+}	$87.43x^{0.9687}$	0.9630

3.2.3. Trends of SW concentrations

Contrary to the increasing trend of pH in WD, the pH in SW showed a significant decreasing trend ($p < 0.0001$; Table 3.4, Figure 3.5 a). The lowest pH (6.35) was recorded in February 2019. The highest was 7.51 in October 2005. A significant increase in the concentrations of SO_4^{2-}, NO_3^-, Ca^{2+}, and DIN was observed (Mann–Kendall Test, $p = 0.007$, $p < 0.0001$, $p = 0.034$, and $p < 0.0001$, respectively; Table 3.4, Figure3.5 b, c, e). The NO_3^- concentration has largely fluctuated since 2014, and higher values over 0.05 mEq L^{-1} have often been recorded. The Ca^{2+} concentration showed a fluctuation similar to NO_3^- since 2014. The NH_4^+ concentration was comparatively low. The Mg^{2+} concentration was relatively steady,

except for the 2019 when there was an abrupt decrease. The trends of SW discharge were not necessarily consistent with those of atmospheric deposition (see chapter 3.1.2.3).

Table 3.4. Trend analysis using the Mann-Kendall test for major-ion concentrations in the SW for the period 2005-2020. Hatched lines represent the significant trends.

Components	Z	*p* value
pH	-5.1039	0.0000
SO_4^{2-}	2.6966	0.0070
NO_3^-	6.6358	0.0000
NH_4^+	1.2806	0.2003
Ca^{2+}	2.1196	0.0340
Cl^-	-0.4535	0.6502
DIN	5.9702	0.0000

A gradual decrease in pH with an increase in the SO_4^{2-} and NO_3^- concentrations in SW at KMR implies that the acidification process of SW has progressed at the KMR. Especially it is significant in the last decade. The leaching of SO_4^{2-} and NO_3^- has contributed to the increase in H^+ leaching in SW during the acidification process (Duan et al., 2011; Garmo et al., 2014; Nakahara et al., 2010).

Underlying mechanisms for acidification are complicated; for example, the acidification process in SW at IJR was regulated by N leaching (Nakahara et al., 2010; Sase et al., 2019), while recovery from acidification was observed with a decrease in SO_4^{2-} concentration in SW at KJK (Sase et al., 2021). In other cases, in China and Japan during the recovery process from acidification, decrease in SO_4^{2-} and NO_3^- concentrations were observed (Duan et al., 2011; Sase et al., 2019, 2021). Since the NH_4^+ concentration was relatively low, DIN changes in SW were mostly regulated by NO_3^-.

Possible “acid shock” was only observed in April 2013, 2014, and 2015 (Figure 3.5a). It is difficult to distinguish the presence of the acid shock for other years, as the snowmelt season at KMR took place from April to May, but only one sample per year was taken during that time. Kobayashi et al. (2013) observed a sudden pH decline with increases in EC and SO_4^{2-} concentration in a river close to

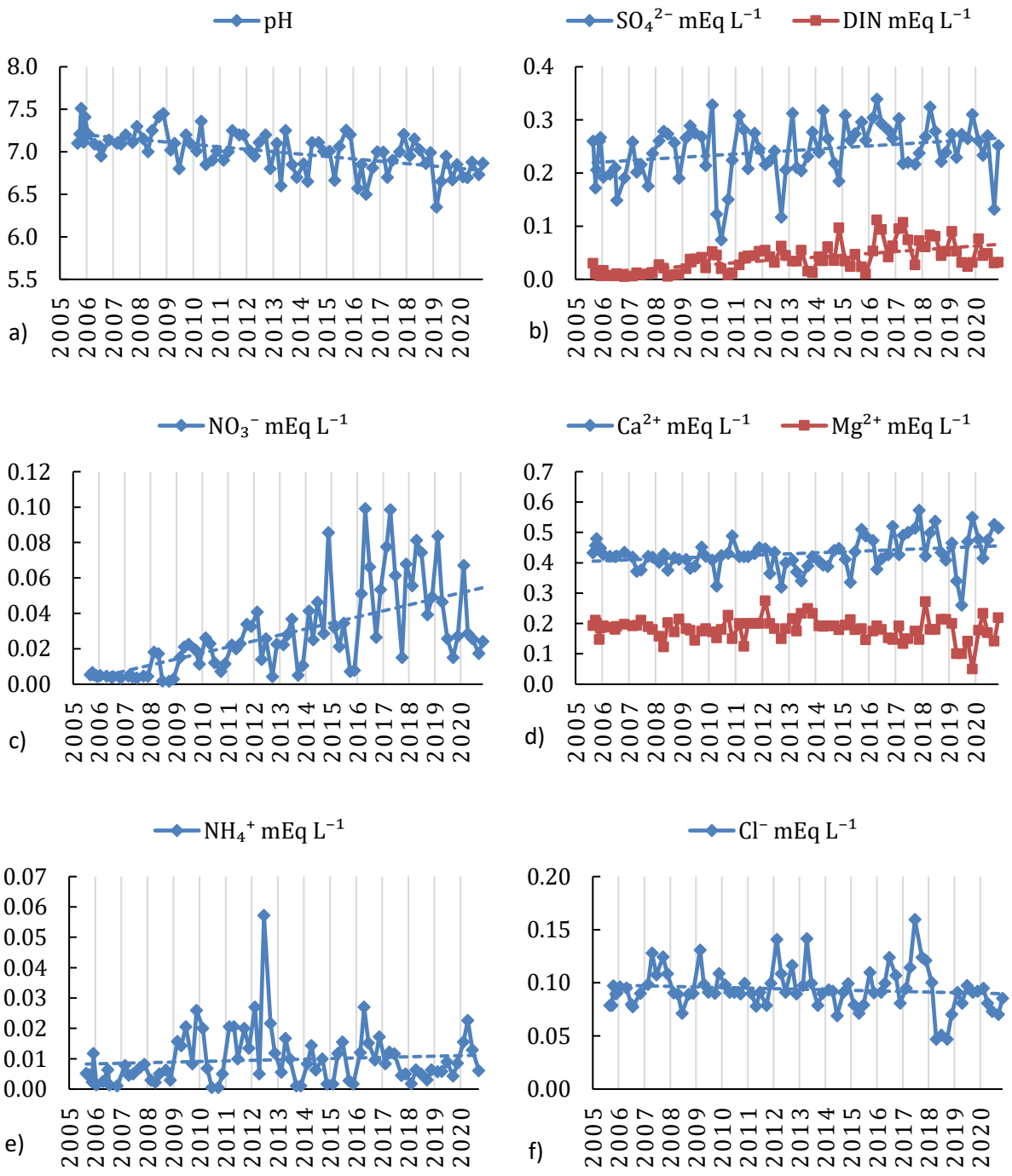

Figure 3.5. Seasonal and interannual variations in the pH values, concentrations of SO_4^{2-} and NO_3^-, concentrations of Ca^{2+}, Mg^{2+} and NH_4^+, in SW during the period 2005–2020. The vertical grid line corresponds to the beginning of each year. (Updated from Zhigacheva et al. 2022)

KJK in Niigata, Japan, where precipitation amounts (mainly as snow) in winter are very high (mean maximum snow depth, 75.8 cm in January). But as shown in Figure 2.3, the precipitation amounts in winter are very low (< 100 mm for November to February) at KMR, suggesting little snow. This also causes difficulty in catching typical snow-melting events that could result in acid shock (Zhigacheva et al. 2022).

3.2.4. Ion ratios

As seen in Figure 3.6, the N/S ratio showed an increasing trend (Mann–Kendall Test, $p < 0.0001$). Especially the increase is stronger since 2009/2010, followed by a rise in values amplitude. That indicates that the DIN concentration in SW has increased faster than that of SO_4^{2-}.

At the same time, the Ca^{2+}/SO_4^{2-} ratio is staying comparatively even with couple of sudden outshoots in 2011 and 2020.

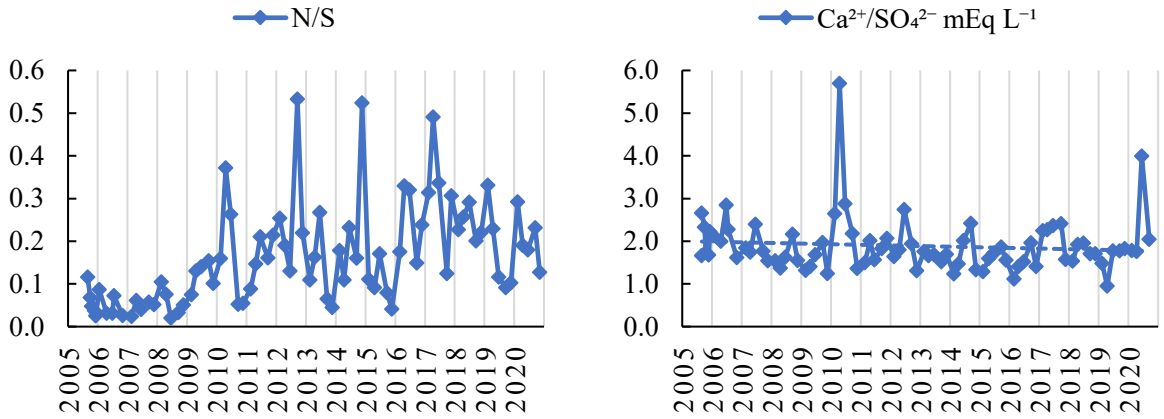

Figure 3.6. Seasonal and interannual variations in the N/S ratios, (i.e., (NO_3^- + NH_4^+)/ SO_4^{2-}) and Ca^{2+} / SO_4^{2-} ratios. (Updated from Zhigacheva et al. 2022)

The relationship between Ca^{2+} and alkalinity is shown in Figure 3.7. During the observational period, the alkalinity showed no specific trend. The data from 2005 to 2009 and from 2010 to 2013 showed similar relationships between the variables, although the regression for the data from 2010 to 2013 was not statistically significant ($R = 0.18$, $p = 0.06$). The regression slope for the data from 2005 to 2009 was gentler than that of the 1:1 line. After 2013, most of the data were plotted above the 1:1 line because of the increase in Ca^{2+}. The regression slope for the data from

2014 to 2020 became steeper than those in the previous period. Except for the 2020, points for the last period are situated above the 1:1 line.

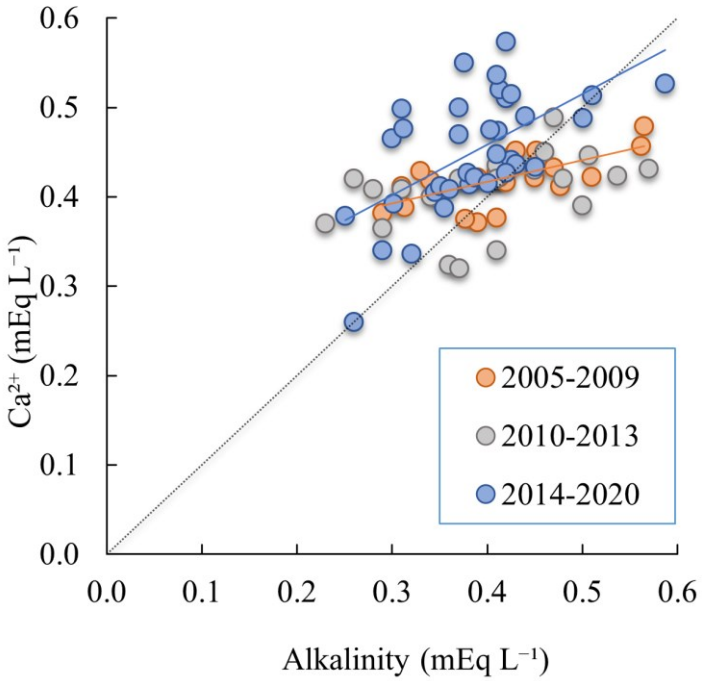

Figure 3.7. Relationship between Ca^{2+} and alkalinity in mEq L^{-1} in SW from 2005 to 2020. Periods 2005 to 2009, 2010 to 2013, and 2014 to 2020, are presented. The thick dotted line shows the 1:1 line. (Updated from Zhigacheva et al. 2022)

Excess of Ca^{2+} leaching into the SW could be another factor that indicates the ongoing acidification at KMR SW. Alongside the increase in SO_4^{2-} and NO_3^- concentrations, Ca^{2+} concentration also showed an increasing tendency (Mann–Kendall test, $p = 0.034$), particularly increase is visible after 2014/2015. Ca^{2+} trend is possibly synchronized with the trends of SO_4^{2-} and NO_3^-. Long-term data from the Hubbard Brook Experimental Forest in the United States clarified that the concentrations of base cations (including Ca^{2+} and Mg^{2+}) in the SW in this region generally increased with those of strong acid anions (SO_4^{2-} and NO_3^-) before the peaks in 1969–1970, in response to acid deposition (Likens et al., 1996). Duan et al. (2011) noted a significant increase in Ca^{2+} concentrations with those of SO_4^{2-} and NO_3^- during river water acidification in the 1990s in China. Atmospheric deposition of acidic substances, such as H_2SO_4, enhanced mobilization of Ca^{2+} in soils due to

cation exchange and mineral weathering, but the acidic substances were only partly neutralized by mobilized Ca^{2+} in acidified rivers (Duan et al., 2011). In the recovery processes from acidification, it has been pointed out that concentrations of base cations, such as Ca^{2+}, decrease in streams or lakes (Garmo et al., 2014; Stoddard et al., 1999; Weyhenmeyer et al., 2019). Thus, changes in Ca^{2+} concentrations are closely related to acidification (Zhigacheva et al. 2022).

It has been suggested that a charge-equivalent proportion between Ca^{2+} concentration and alkalinity is decoupled due to an increase in Ca^{2+} concentration in the anthropogenic acidification process (Weyhenmeyer et al., 2019). At KMR, the regression slope of Ca^{2+} against alkalinity was gentler than the 1:1 line in the years from 2005 to 2009, as shown in Figure 3.7. However, an imbalance between Ca^{2+} concentration and alkalinity became more obvious with an increase in Ca^{2+} concentration in 2014–2020, deviating from the 1:1 line.

3.2.5. Seasonal trends (cold and warm seasons)

Changes in the SW discharge and fluxes of SO_4^{2-}, NO_3^-, and Ca^{2+} calculated for the 7 years with available daily discharge data by the L-Q method in cold and warm seasons are shown in Figure 3.8. The seasons are the same as for the WD: cold season from October to March, and warm season from April to September. But for SW the cold season was calculated for the same year and not as consequent season from one year to the following.

It can be suggested that compounds discharge fluxes are much higher during the warm season, which is mostly related to the increase of SW discharge. In recent years, following the increase in precipitation amounts during the warm season, the SW discharge is also increasing. Along with that, increase in compounds fluxes can be seen starting from the 2010s. In contrast with the decrease in compounds concentrations in last two years (2019 and 2020), compounds discharge fluxes continue to increase. The reason for that should also lay in the calculation method which is based on the water discharge values. Compounds output fluxes (Figure 3.8 b-d) are similar to the SW discharge flux (Figure 3.8 a). Probably, the recent increase

in SW fluxes of SO_4^{2-} and DIN can be attributed to the increased discharge in the warm season (Zhigacheva et al. 2022).

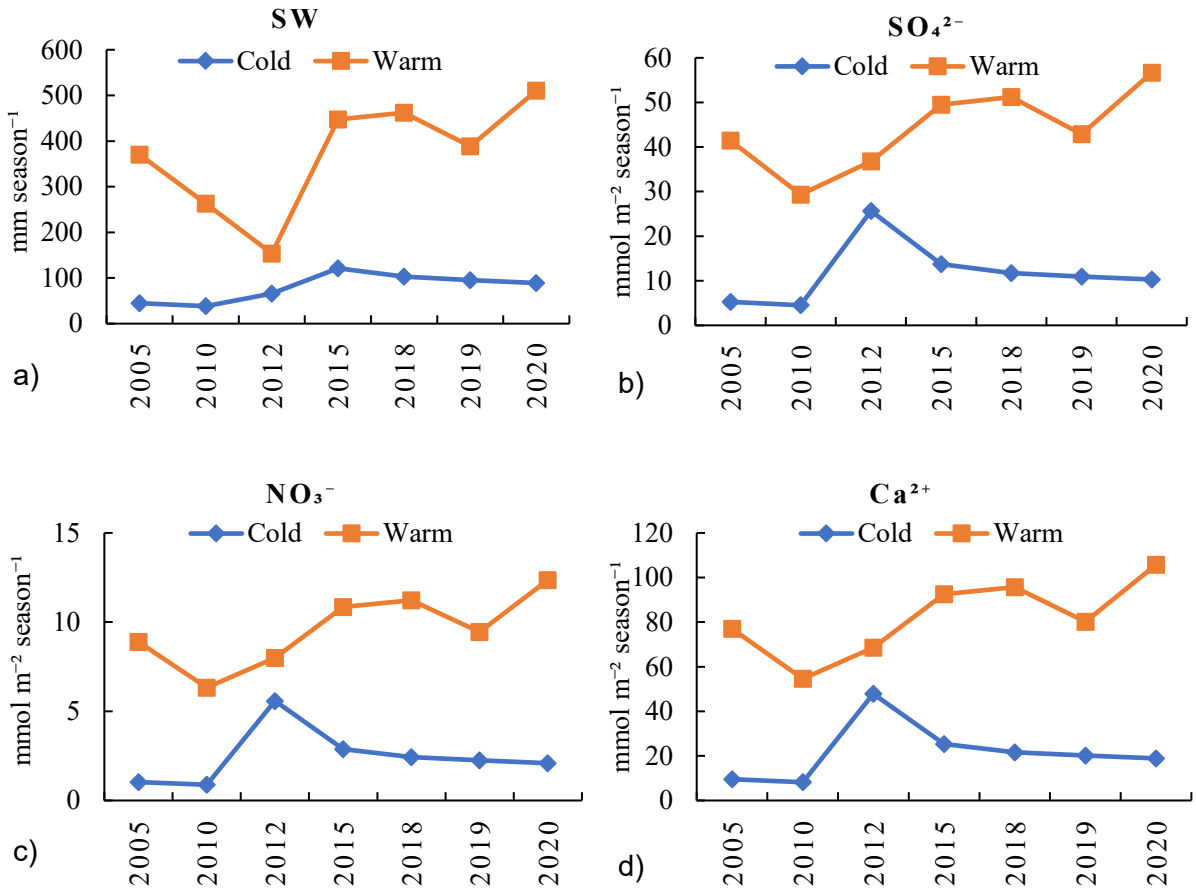

Figure 3.8. The SW discharge and fluxes of SO_4^{2-} and NO_3^- and Ca^{2+} during the cold and warm seasons of monitoring years. The fluxes were estimated by the L-Q method for 7 years with daily discharge data available. (Updated from Zhigacheva et al. 2022)

3.2.6. Water regime season trends

Since the SW has been collected five times per year: in February, April, June, September, and November, the trend analysis was performed using the Mann–Kendall test for each season to determine its seasonal dependency, representing different water regime seasons (Table 3.5). Those months can be considered as specific water regime seasons. February - extremely low water discharge levels. April - snow melting period and the start of the spring flood. June and November are periods of the base flow. September - increasing discharge (Zhigacheva et al. 2022).

For present calculations years 2005 and 2006 are not included as the sampling periods were not established at that time yet. In 2005 sampling was performed at August, September, October, November, and December. In 2006 – in January, April, June, July, and November.

Results of the Mann–Kendall Test are presented in Table 3.5. Decreasing trends in pH were observed in February and September ($p = 0.003$ and $p = 0.015$, respectively). The NO_3^- concentration showed an increasing trend for February, April, and June ($p = 0.0001$, $p = 0.0062$, $p = 0.0035$, respectively). Two other months for NO_3^- have increasing trends of low significance ($p < 0.1$). Increasing trends for Ca^{2+} are presented for individual months too – in February, September, and November.

Table 3.5. Trend analysis using the Mann-Kendall test for major-ion concentrations in the SW for each sampling month. Hatched data show significant decreasing and increasing trends. (Updated from Zhigacheva et al. 2022)

	pH		**SO_4^{2-}**		**NO_3^-**		**NH_4^+**		**Ca^{2+}**	
	Z	***p***	**Z**	***p***	**Z**	***p***	**Z**	***p***	**Z**	***p***
February	-2.98	0.003	0.00	1.0000	3.94	0.0001	0.49	0.6206	2.31	0.0211
April	-1.59	0.111	0.88	0.3811	2.74	0.0062	-0.38	0.7011	0.55	0.5841
June	-1.54	0.123	1.20	0.2284	2.92	0.0035	1.09	0.2736	1.64	0.1005
September	-2.43	0.015	0.00	1.0000	1.70	0.0892	0.66	0.5099	2.08	0.0375
November	-1.87	0.062	1.86	0.0627	1.86	0.0627	-0.44	0.6614	2.03	0.0425

To estimate the relationship between SW discharge and major ions and pH concentrations, the Spearman's rank correlation test was performed. The correlation coefficients between the SW flow rate and ion concentrations in each sampling month for the period from 2007 to 2020 are listed in Table 3.6. Significant positive correlations with the SW flow rate were observed for NO_3^- and DIN in June. NH_4^+ has a significant positive correlation between SW flow and concentration in November and for the all-season data. For other compounds correlation is not significant, meaning that other factors have more influence on compounds concentrations.

Table 3.6. Spearman's rank correlation coefficients between the SW flow rate and ion concentrations in each sampling month for the period from 2007 to 2020 (Updated from Zhigacheva et al. 2022).

	SO_4^{2-}	NO_3^-	NH_4^+	Ca^{2+}	Cl^-	DIN	pH
February	0.25	0.35	-0.08	-0.02	-0.53	0.21	-0.14
April	0.01	-0.39	0.28	-0.23	0.22	-0.23	0.16
June	0.54	0.62	0.49	-0.22	-0.22	0.68	0.08
September	-0.32	0.00	0.13	-0.35	0.38	0.53	0.15
November	-0.06	0.26	0.63	-0.24	0.02	0.29	-0.03
All-season	-0.23	0.01	0.35	-0.25	0.02	0.17	0.09

Note. Blue color, $p < 0.05$

To estimate trends in discharge fluxes for individual months is hard because the amount of sampling is insufficient. Thus, the 3-years moving flux-weighted means were calculated for every water regime season. Results of Mann-Kendall Test estimation for those rows are presented in Table 3.7. And a visual representation of those trends is shown in Figure 3.9.

Table 3.7. SW trend analysis using the Mann-Kendall test for the 3-years moving flux-weighted means for major-ion concentrations in each respective sampling months

	pH		SO_4^{2-}		NO_3^-		NH_4^+		DIN		Ca^{2+}	
	Z	p	Z	p	Z	p	Z	p	Z	p	Z	p
February	-2.47	0.0133	0.21	0.8370	4.18	0.0000	-1.03	0.3037	3.77	0.0002	1.99	0.0467
April	-2.81	0.0049	2.40	0.0164	1.71	0.0865	-0.89	0.3727	1.71	0.0865	1.71	0.0865
June	-0.83	0.4073	1.99	0.0467	3.09	0.0020	0.62	0.5371	3.09	0.0020	2.13	0.0335
September	-1.86	0.0629	0.75	0.4507	-0.48	0.6312	0.34	0.7317	-1.85	0.0641	2.67	0.0075
November	-1.65	0.0990	2.26	0.0236	2.81	0.0049	-2.13	0.0335	1.85	0.0641	2.40	0.0164

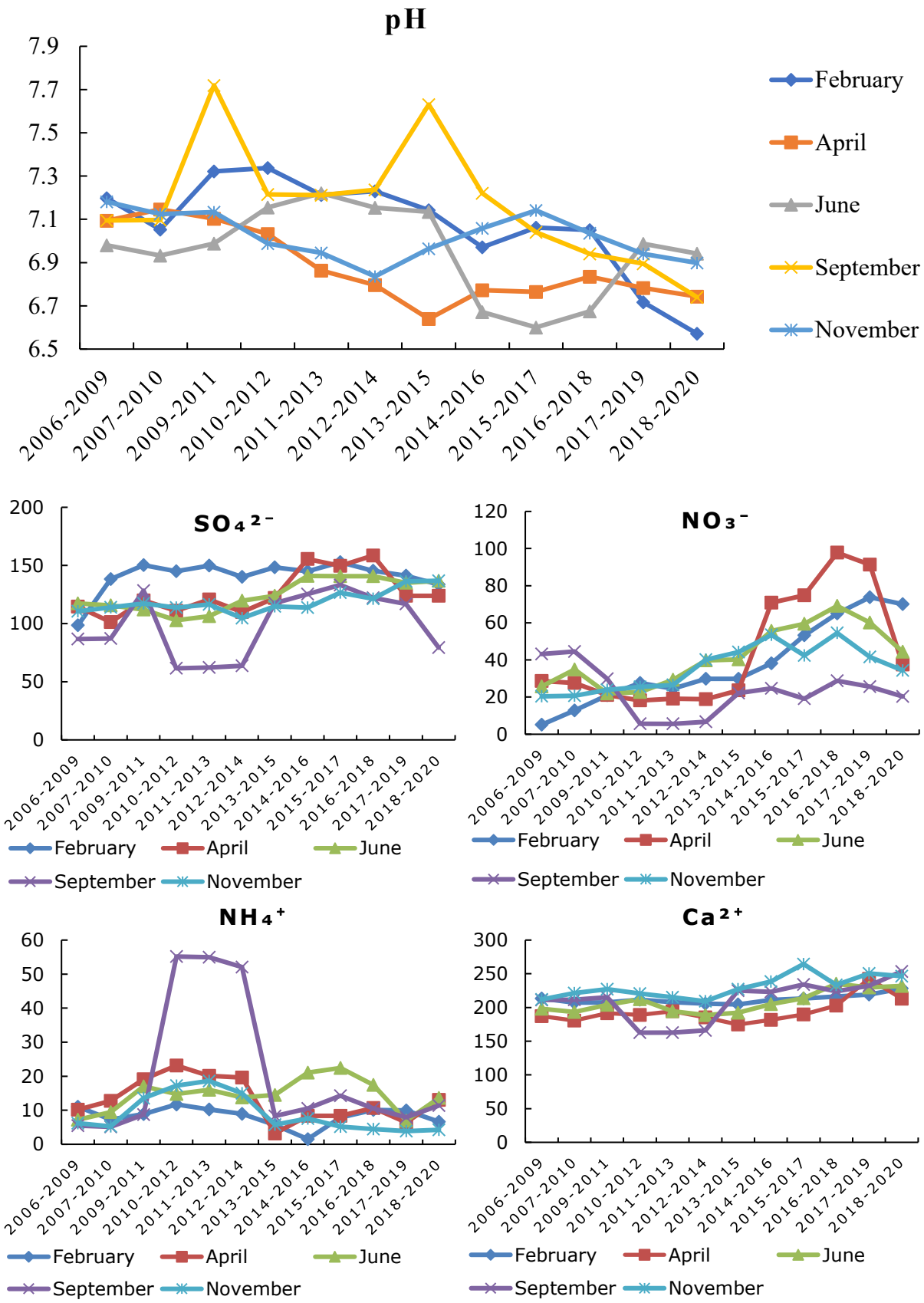

Figure 3.9. SW 3-years moving flux-weighted means for pH and ions in each respective sampling months (unit: pH: pH-values; ions: mmol m^{-3})

Statistically significant decrease in pH is monitored in February and April. SO_4^{2-} is increasing in April, June, and November. NO_3^- is increasing in February, June, and November. Ca^{2+} is increasing in every water regime season except for April. NH_4^+, in contrary is decreasing in November.

However, significant trends for pH decrease and SO_4^{2-}, NO_3^-, and Ca^{2+} increase can be seen not only during the warm season, but also in February and November. Thus, increase in deposition during the warm season does not completely explain acidification processes of the SW.

Warm and humid periods possibly play a significant role in the acidification of the KMR. Climatic changes in the region may be partly responsible for the changes in SW concentrations. According to the Roshydromet (2020), in the Russian Far East climate warming continues in all seasons except for winter. And climate plays a significant role in the processes of acidification (see chapter 1). Increase in precipitation lead to the escalated mobilization of acidifying agents from the catchment internal sources and amplified material discharge (Mitchell et al., 2013; Mitchell & Likens, 2011; Sase et al., 2017; Sase et al., 2019; Shao et al., 2021). As abiotic and biotic processes are also dependent on the temperature many mechanisms related to the N and S biocycles will also depend on climate changes (Houle et al., 2020). Warm and humid conditions lead to higher rates of N mineralization and nitrification. High precipitation results in the movement of N from soils and groundwater to the SW (Fang et al., 2011; Ohte et al., 2001).

3.3. Input-Output balance

For the input-output budget calculation it was assumed: the input consists of total (dry and wet) deposition while the output is presented solely by the discharge with the SW.

The input and output balances for the S, N, Cl, and Ca compounds are shown as the mean values for six years in Figure 3.10. As was mentioned before, the exact calculation of compounds discharge fluxes is hard due to the insufficient amount of sampling in a year. Thus, discharge fluxes are calculated and presented by two

different methods: I-R and L-Q. Calculations by L-Q method are possible only for years with daily SW discharge data available. I-R method is not applicable for the 2005 as samplings at that year started only from August. Thus, all the calculations were performed for six years where all the methods could be implemented: 2010, 2012, 2015, 2018, 2019, and 2020.

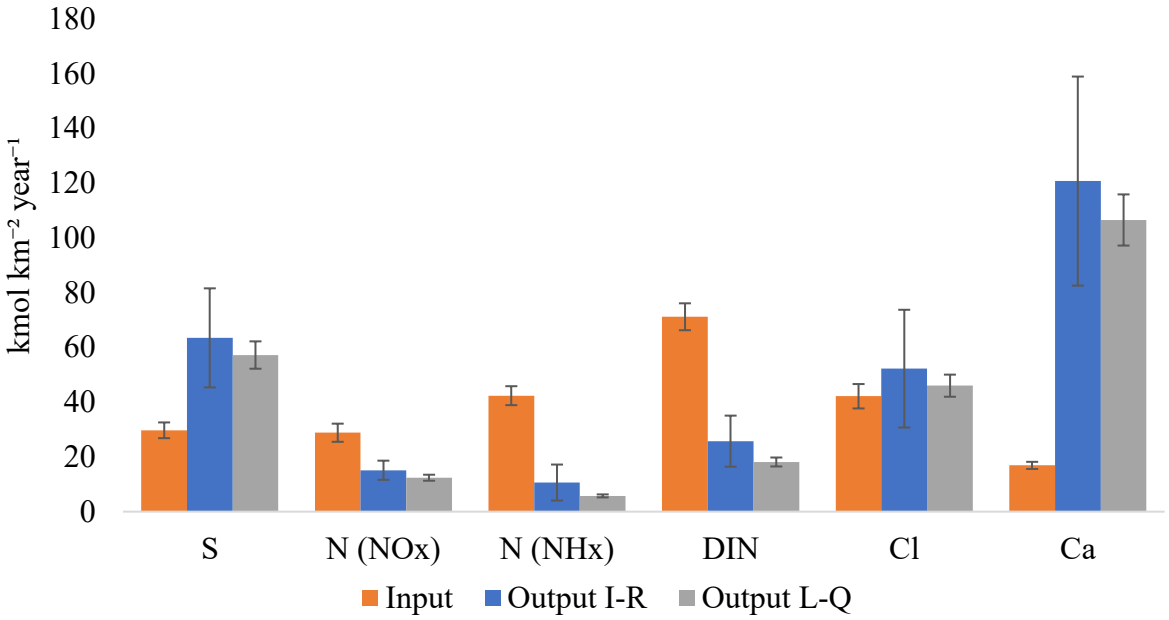

Figure 3.10. Input and output balances for S, N, Cl and Ca in KMR. The mean values for 2010, 2012, 2015, 2018, 2019, and 2020 are shown. Input, total atmospheric flux by WD and DD; Output I-R, flux estimated by the I-R method; Output L-Q, flux estimated by the L-Q method. Bars represent standard errors. (Updated from Zhigacheva et al. 2022)

Although output calculated by I-R method tends to be higher, compared to L-Q method results, the difference between them is not very high.

The mean outputs of S by both methods were higher than the input, and the discrepancy was typical for these calculated years except for 2010. For N compounds, the mean outputs were considerably lower than the inputs. The mean outputs of Cl were relatively well balanced to the input. The mean outputs of Ca were significantly higher than the input.

Although there are still uncertainties in the estimation of both input and output, the input and output of Cl, considered one of the representative inert ions in forest ecosystems, were relatively well balanced.

The observed discrepancy for S with output higher than input is typical for some recovering catchments subject to high emissions and the deposition of pollutants (Zhigacheva et al. 2022). The high S output has been attributed to the mobilization of formerly accumulated S in soils of the catchment areas in Europe (Novák et al., 2000; Vuorenmaa et al., 2017). Moreover, the importance of internal sources, including geological S, has been suggested in the United States (Mitchell and Likens, 2011; Mitchell et al., 2013), Japan (Sase et al. 2019), and Sabah, Malaysia (Yamashita et al., 2014). The leaching of S, such as weathering from minerals, mineralization of organic S, and desorption of S, are largely influenced by humid conditions (Mitchell and Likens, 2011). Mineral weathering may contribute to the significant increase in Ca^{2+} concentration in SW. Part of the Ca^{2+} was released into SW with acidification by atmospheric SO_4^{2-} input (Weyhenmeyer et al., 2019).

Chapter 4. Sea of Japan region (Kajikawa and Ijira)

4.1. Air mass trajectories

For one of the monitoring sites in Japan, backward trajectories by the HYSPLIT resources were estimated. Ending points time is the same as for the frequency calculations at KMR. Every calculation oversees the 72-hours trajectories with ending points at 3 different heights: 100m, 500m, and 1000m.

For trajectories ending at KJK, it was found that quite a lot of trajectories during the cold season are coming from the direction of KMR crossing the Sea of Japan. Two examples of winter backward trajectories are presented in Figure 4.1. All the 24 maps can be found in Appendix 3.

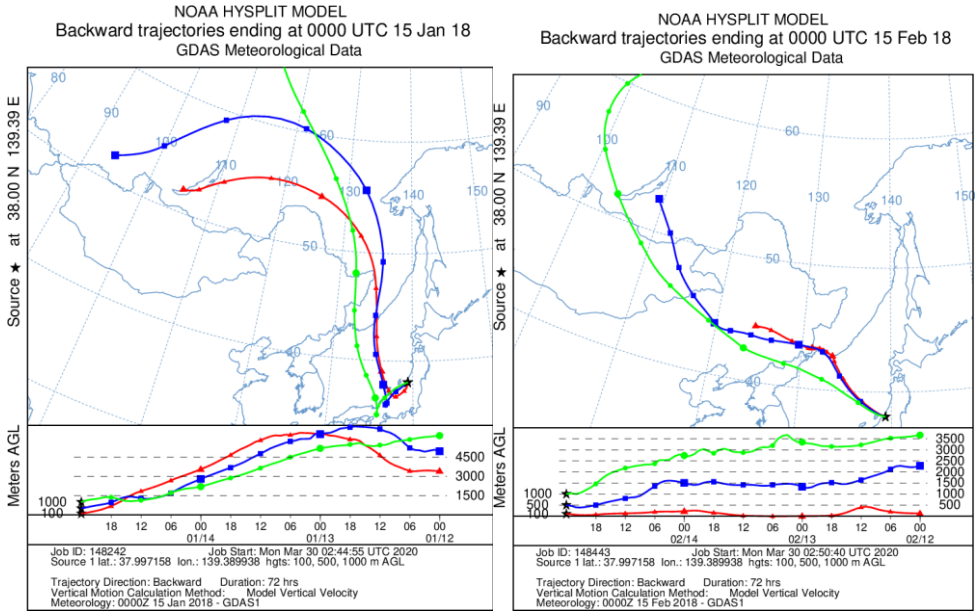

Figure 4.1. 72-hours Back-trajectories coming to KJK in 2018. Ending dated are January 15 (left) and February 15 (right)

4.2. Reasons for comparison and sites description

Two Japanese sites, the Kajikawa site (KJK) and the Ijira site (IJR), were selected for comparison with the KMR based on their geographical situation and characteristics (see Figure 2.1). Situated comparable close geographically and belonging to the Sea of Japan region, they are all presumably were influenced by acid deposition. At the same time, climate of those territories differs greatly.

Difference can be also found in vegetation, bedrock materials and soils, as well as domestic sources of pollution. For both Japanese sites, long term data on deposition monitoring is available that makes the comparison possible.

The KJK (37° 59′ N, 139° 23′ E) is a small, forested catchment (approximately 0.0384 km) in the Niigata Prefecture, Japan, near the Sea of Japan coast. The catchment area is fully covered by forest, mostly 50-year-old Japanese cedar trees (*Cryptomeria japonica* D. Don), and the dominant soil type is Cambisols (Sase et al., 2008, 2021). The IJR (35° 34′ N, 136° 41′ E) is the EANET catchment monitoring site (area, approx. 2.98 km) located on the Pacific side in Gifu Prefecture, central Japan (Nakahara et al., 2010; Sase et al., 2019), while the effects of transboundary air pollution through the Sea of Japan have also been suggested (Inomata et al., 2019). The dominant soil type is Cambisols, while the predominant vegetation is the Japanese cypress (*Chamaecyparis obtusa* Sieb. & Zucc., 49% of the catchment area).

4.3. Comparison of deposition and discharge levels

Deposition levels at KMR are comparatively lower than at IJR and KJK. The latest 5 years mean fluxes of WD were lower at KMR than at KJK and IJR, except for the Ca^{2+} flux which was higher at KMR than at IJR. At the same time, SW concentrations at KMR appear to be higher. The latest 5 years mean concentrations of SO_4^{2-}, NH_4^+, and Ca^{2+} in SW are presented in Table 4.1.

Table 4.1. 5-years means of rainwater deposition and concentration in SW at KMR, KJK, and IJR (Zhigacheva et al. 2022)

		Wet deposition (mmol m^{-2} $year^{-1}$)			Stream water (μEq L^{-1})		
		KMR	KJK	IJR	KMR	KJK	IJR
SO_4^{2-}	2015–2019	23.1	43.0	31.1	270	98.2	130
NO_3^-	2015–2019	23.6	51.5	45.1	48.7	51.5	24.8
NH_4^+	2015–2019	27.1	34.7	38.6	8.2	0.89	0.02
Cl^-	2015–2019	27.3	277	54.5	91.8	410	55.4
Ca^{2+}	2015–2019	13.2	20.0	6.41	451	357	132

N is lately though to be getting significant role in acidification processes. Especially the problem of N leaching is under the scope of interest. The relationships between the 5 years moving means of the DIN fluxes by precipitation and NO_3^- concentrations in SW at KMR, KJK, and IJR were estimated (Figure 4.2). The mean NO_3^- concentration in SW greatly increased at KMR, while the mean DIN flux by precipitation slightly increased but did not change greatly. For the same periods, the NO_3^- concentration in SW decreased with the DIN flux by precipitation at IJR, while the NO_3^- concentration in SW increased and then became stable or rather slightly decreased at KJK.

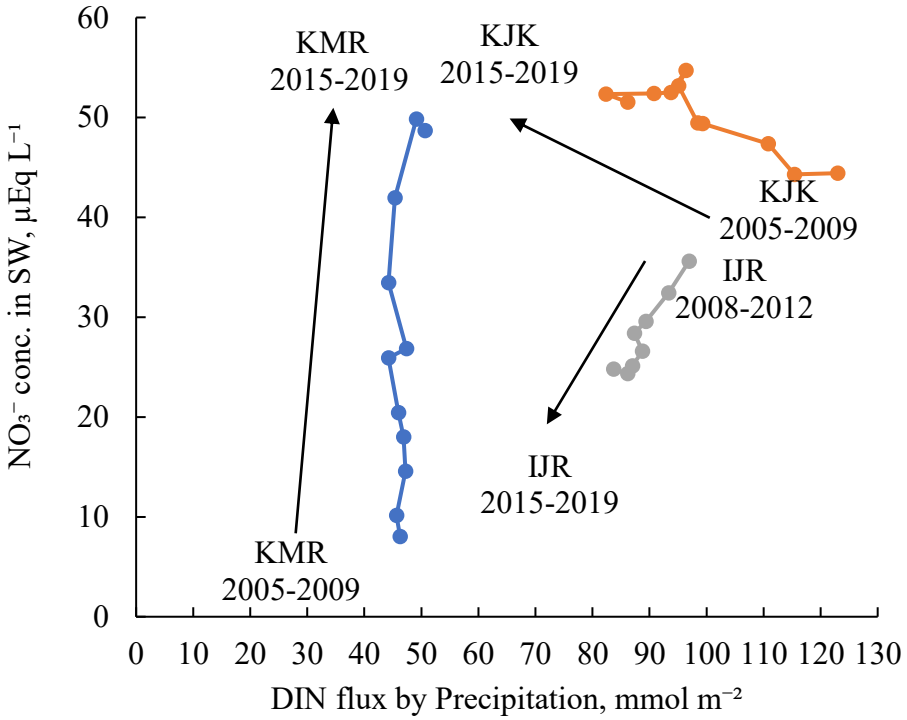

Figure 4.2. The relationship between the 5 years moving means of DIN flux by rainwater and NO_3^- concentration in SW at KMR, KJK, and IJR (Zhigacheva et al. 2022)

IJR was reported firstly as a catchment acidified by atmospheric deposition in Japan, in which climatic anomalies, such as cool summer and severe drought, contributed largely to changes in the biogeochemical cycles (Nakahara et al., 2010; Yamada et al., 2007). However, recovery from acidification and N saturation has

progressed recently (Sase et al., 2019). While KJK is considered under recovery from acidification, the S output was higher than the input over recent years due to slower and weaker ecosystem response to changes in atmospheric inputs (Sase et al., 2021).

The discrepancy in the S balance appears similar to the phenomena in KMR. However, the main S source for SW has not yet been identified at the KMR. In the future, S isotopic analysis can be applied to rainwater and SW at KMR to identify possible S sources and estimate their contributions.

At both IJR and KJK, changes in atmospheric deposition partly reflect the regional emission trends (Sase et al., 2021), while such a relationship was not clear at KMR. This is probably because IJR and KJK are located downwind of the Asian continent, while KMR is located in the north edge of the continent, close to various local/regional emission sources. There were lower atmospheric fluxes at KMR in comparison to KJK and IJR. The 5 years mean DIN flux by precipitation was almost half that of KJK and IJR (see Figure 4.2). With high levels of DIN flux by precipitation, NO_3^- concentration in SW at IJR decreased significantly in response to a decrease in the atmospheric deposition.

For KJK, the SW response to the atmospheric deposition was not so simple: NO_3^- concentration in the SW first increased with the decreasing DIN flux and then became stable. For KMR, by contrast, even under low levels of atmospheric deposition, the mean NO_3^- concentration substantially increased with a slight increase in the DIN flux by precipitation. It is suggested that the change in seasonal precipitation patterns mentioned above contributed to N leaching from the forest ecosystems, in addition to DIN deposition (Zhigacheva et al. 2022).

As for the phenomena observed at KJK, it was suggested that maturation of Japanese cedar trees and forest management largely influenced N leaching from the plantation forests, in addition to DIN deposition (Sase et al., 2022). As Yang & Chiwa (2021) noted, the relatively low N uptake by Japanese cedar could also contribute to high N leaching in plantations. The predominant tree species is the Japanese cypress at IJR. Conversely, the catchment area of KMR is mainly covered

by broadleaf forest, while the pine trees are partly included. Moreover, the stand ages at IJR and KJK are approximately 50 years old (Sase et al., 2022), while the age of the broadleaf forest at KMR in the nature reserve was not clear. These factors may influence N retention in forest ecosystems. It is suggested that forest conditions, such as tree species composition and tree stand age, should be taken into consideration when evaluating N leaching mechanisms in forest catchments (Zhigacheva et al. 2022).

Chapter 5. Overall discussion

As a possible influence of anthropogenic emission sources on atmospheric environment in the study site, the concentration of gaseous HCl showed a clear peak in 2011 with the following gradual decrease. When SW acidification was observed, the fluxes of S and DIN started increasing again, and the anthropogenic Cl flux increased.

In the Northeast Asian region, high emissions of SO_2 and NOx (and high atmospheric deposition) contributed to the acidification of SW (e.g. Duan et al. 2011), while the SW has been gradually recovering from acidification with a decrease in emissions (e.g. Qiao et al., 2016; Sase et al., 2019, 2021). Although the aforementioned atmospheric conditions at the Primorskaya site may partly explain acidification phenomena at KMR, the question remains to be answered as to why the increases in the leaching of SO_4^{2-} and NO_3^- started in the mid-2010s.

The recent increase in NO_3^- concentration was evident for KMR SW, even though the values fluctuated greatly. It has been suggested that N leaching plays a significant role in the acidification process. This is consistent with the trends in Europe, the USA, and East Asia, where SO_4^{2-} emissions have declined significantly over the past decades (Bouwman et al., 2002; Duan et al., 2011). With a decline in S deposition, recovery processes can be prolonged due to an increase in N deposition (Duan et al., 2011; Sase et al., 2021).

The suggested thresholds of N deposition for N leaching to SW are estimated as 10 kg N ha^{-1} $year^{-1}$ (Wright et al., 1995), 7 kg N ha^{-1} $year^{-1}$ (Aber et al., 2003), and 5 kg N ha^{-1} $year^{-1}$ (Fang et al., 2011) for Europe, the United States, and East Asia, respectively. Fang et al. (2011) pointed out that warm and humid conditions accelerate N leaching from forest ecosystems in East Asia. It could be applied not only to forest ecosystems in the boreal zone under a changing climate. The mean DIN flux by WD at the Primorskaya site was 6.5 kg N ha^{-1} $year^{-1}$, and the estimated total deposition by WD and DD was 10 kg N ha^{-1} $year^{-1}$ for the observational period from 2005 to 2019, which were larger than the threshold for East Asia (Zhigacheva et al. 2022).

The recent increase in precipitation amounts in the warm season and higher contributions of the warm-season atmospheric deposition resulted in the recent acidification of SW. Additionally, leaching of DIN (including NO_3^- and NH_4^+) was accelerated by the increased SW flow in the warm season. Warm and humid periods possibly play a significant role in the acidification of the KMR. Climatic changes in the region may be partly responsible for the changes in SW concentrations (Zhigacheva et al. 2022). According to a report on climate features in the territory of the Russian Federation in 2019 (Roshydromet, 2020), climate warming continues in the Russian Far East in all seasons except winter. Increasing precipitation is also evident but does not exceed 5% per 10 years. Changes in precipitation amounts and patterns play a role in the mobilization of SO_4^{2-} from internal sources into the SW (Mitchell et al., 2013; Mitchell & Likens, 2011; Sase et al., 2017). Warm and humid conditions lead to higher rates of N mineralization and nitrification. High precipitation results in the movement of N from soils and groundwater to the SW (Fang et al., 2011; Ohte et al., 2001).

However, significant trends for pH decrease and SO_4^{2-}, NO_3^-, and Ca^{2+} increase can be seen not only during the warm season, but also in February and November. Means the changes in deposition do not completely explain acidification processes of the SW. The mechanism of material discharge and SW acidification during the cold period should yet be studied.

Chapter 6. Conclusions

The progress of SW acidification at KMR over the past 16 (2005-2020) years was assessed based on the EANET atmospheric deposition and meteorological data. Acidification of KMR SW is still proceeding. The acidification is accompanied by an increase in SO_4^{2-} and NO_3^- concentrations. The Ca^{2+} concentrations are also increasing while alkalinity staying relatively stable, resulting in deviation of their ratio from the 1:1 balance, which also indicate the acidification process.

The recent increase of S, DIN and Cl fluxes contributed partly to the acidification. Because of limited material flows during the cold season, the increase in precipitation amount in the warm season appears to significantly alter biogeochemical processes in forest ecosystems.

The recent increase in discharge fluxes of SO_4^{2-} and NO_3^- could be attributed to the rise of precipitation amount during the warm season and to the following overall increase in SW discharge. Also, discharge in the warm season could be enhanced by the increased WD.

In the Far East of Russia, soil and SW are predominately frozen in winter, suggesting limited material flows during the cold season; therefore, the increase in precipitation amount in the warm season appears to significantly alter biogeochemical processes in forest ecosystems.

Mobilization of S and N from internal sources of catchment areas, such as soil where air pollutants have accumulated during the previous period, can affect SW concentrations and fluxes. Mobilization of S and Ca could also be a reason for discrepancy in input-output balance of those elements.

Even during the cold season, including February and November, we can observe decrease in pH and increase in major acidifying ions, meaning that increase in precipitation and deposition fluxes are not the sole reason of SW acidification.

Although in 2019 and 2020 the decreases in SO_4^{2-} and NO_3^- concentrations were observed under low fluxes of atmospheric deposition, it is premature to conclude that KMR has started recovering from acidification.

Based on comparison with KJK and IJR, which are recovering from the N leaching, KMR even with lower deposition level seems to be sensitive to acidification.

There are still a lot of problems to be studied concerning the acidification process at KMR. The interlinkage between air pollution and climate change should be carefully assessed, particularly in relation to the recovery process from acidification. Factors like vegetation and soil influence should be studied in the relation to the acidification process at KMR. For understanding the sources of excess S discharge into the SW, methods like isotopic analysis could be implemented. Further research on the sources of pollution in relation to the long-range air transport should be studied.

Taking into consideration increasing precipitation during the warm season, the contributions of the WD fluxes during the warm season has increased, reflecting the climatic conditions. In future, the acceleration of material flows in warming winters should also be taken into consideration.

Overall, the detailed mechanisms of SW acidification specific for KMR should be discussed more.

Appendix

Appendix 1. Results of trajectory frequencies analysis by HYSPLIT in 2018 for every air sampling event.

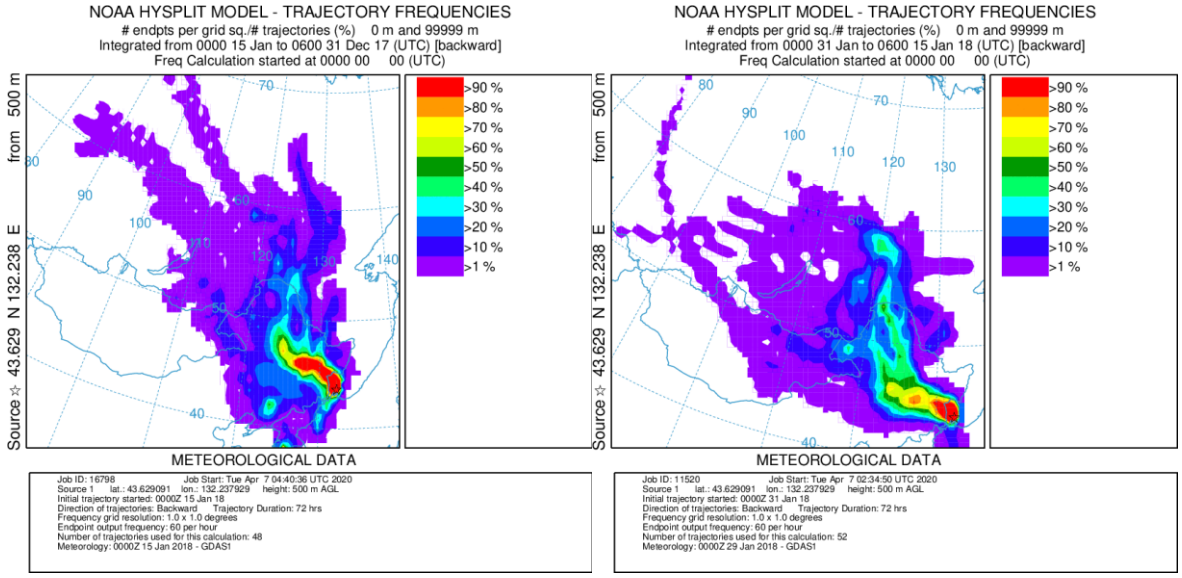

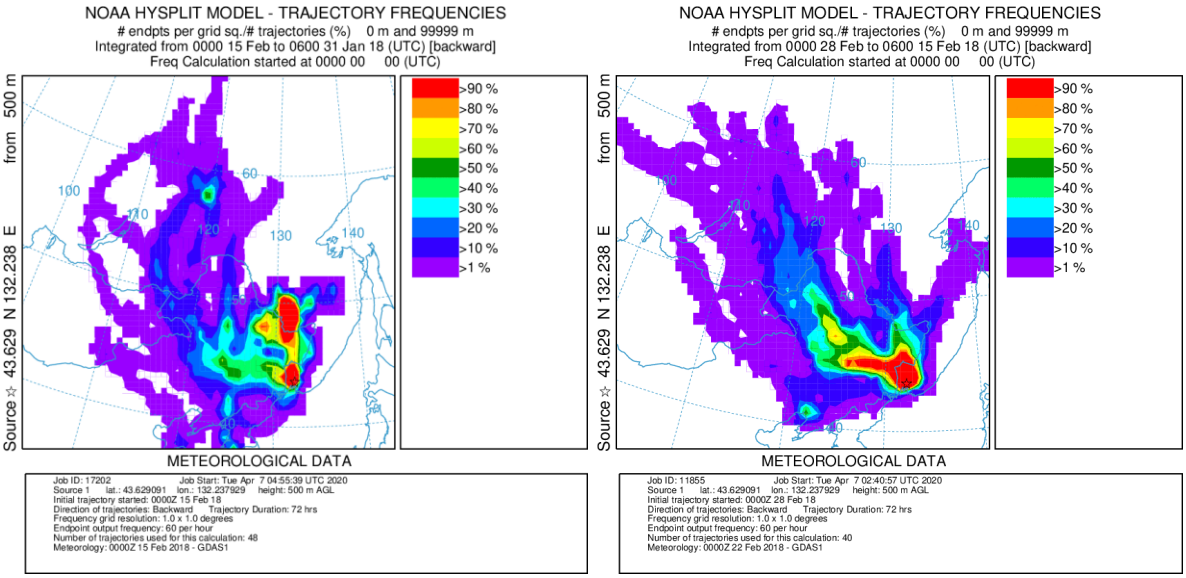

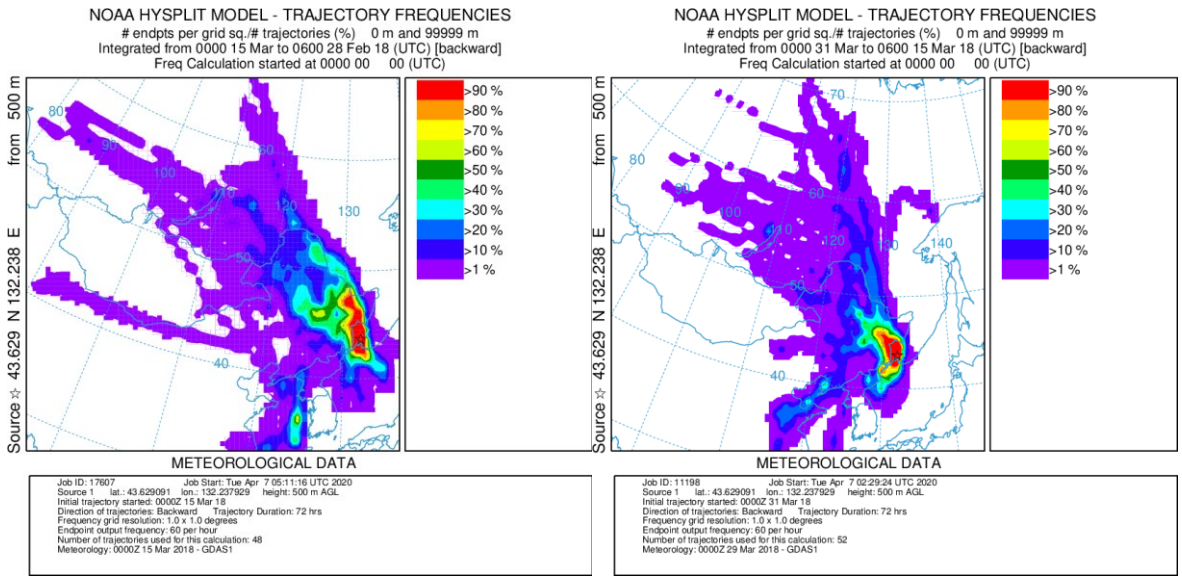

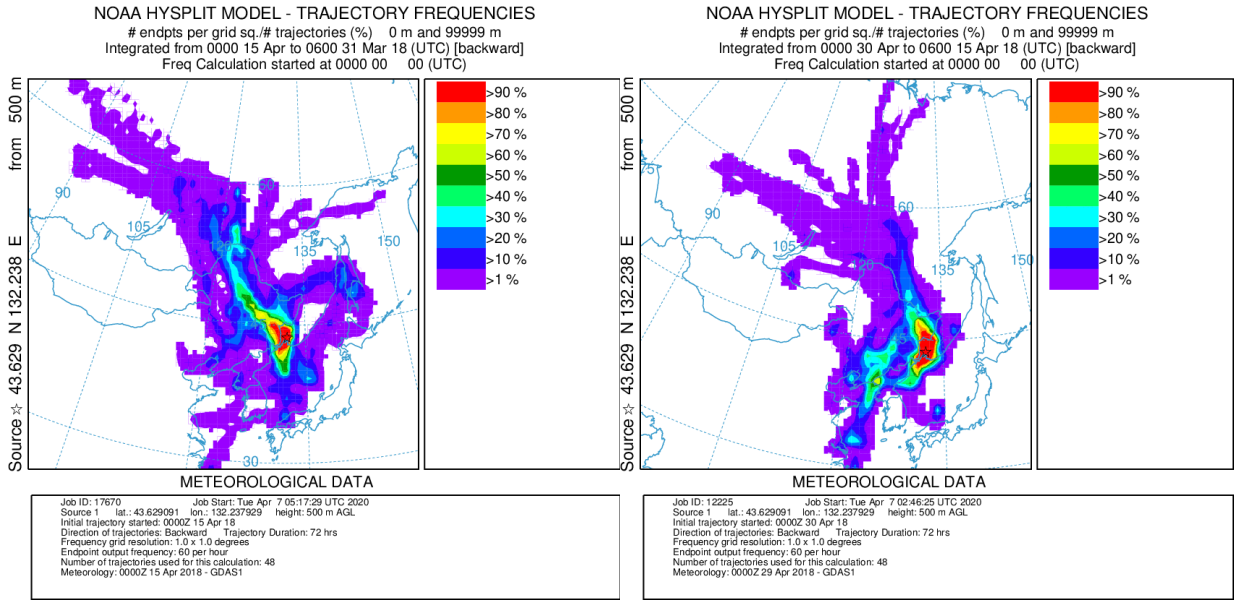
NOAA HYSPLIT MODEL - TRAJECTORY FREQUENCIES
endpts per grid sq./# trajectories (%) 0 m and 99999 m
Integrated from 0000 15 Apr to 0600 31 Mar 18 (UTC) [backward]
Freq Calculation started at 0000 00 00 (UTC)
Source ☆ 43.629 N 132.238 E from 500 m
>90 %
>80 %
>70 %
>60 %
>50 %
>40 %
>30 %
>20 %
>10 %
>1 %
METEOROLOGICAL DATA
Job ID: 17670 Job Start: Tue Apr 7 05:17:29 UTC 2020
Source 1 lat.: 43.629091 lon.: 132.237929 height: 500 m AGL
Initial trajectory started: 0000Z 15 Apr 18
Direction of trajectories: Backward Trajectory Duration: 72 hrs
Frequency grid resolution: 1.0 x 1.0 degrees
Endpoint output frequency: 60 per hour
Number of trajectories used for this calculation: 48
Meteorology: 0000Z 15 Apr 2018 - GDAS1

NOAA HYSPLIT MODEL - TRAJECTORY FREQUENCIES
endpts per grid sq./# trajectories (%) 0 m and 99999 m
Integrated from 0000 30 Apr to 0600 15 Apr 18 (UTC) [backward]
Freq Calculation started at 0000 00 00 (UTC)
Source ☆ 43.629 N 132.238 E from 500 m
>90 %
>80 %
>70 %
>60 %
>50 %
>40 %
>30 %
>20 %
>10 %
>1 %
METEOROLOGICAL DATA
Job ID: 12225 Job Start: Tue Apr 7 02:46:25 UTC 2020
Source 1 lat.: 43.629091 lon.: 132.237929 height: 500 m AGL
Initial trajectory started: 0000Z 30 Apr 18
Direction of trajectories: Backward Trajectory Duration: 72 hrs
Frequency grid resolution: 1.0 x 1.0 degrees
Endpoint output frequency: 60 per hour
Number of trajectories used for this calculation: 48
Meteorology: 0000Z 29 Apr 2018 - GDAS1

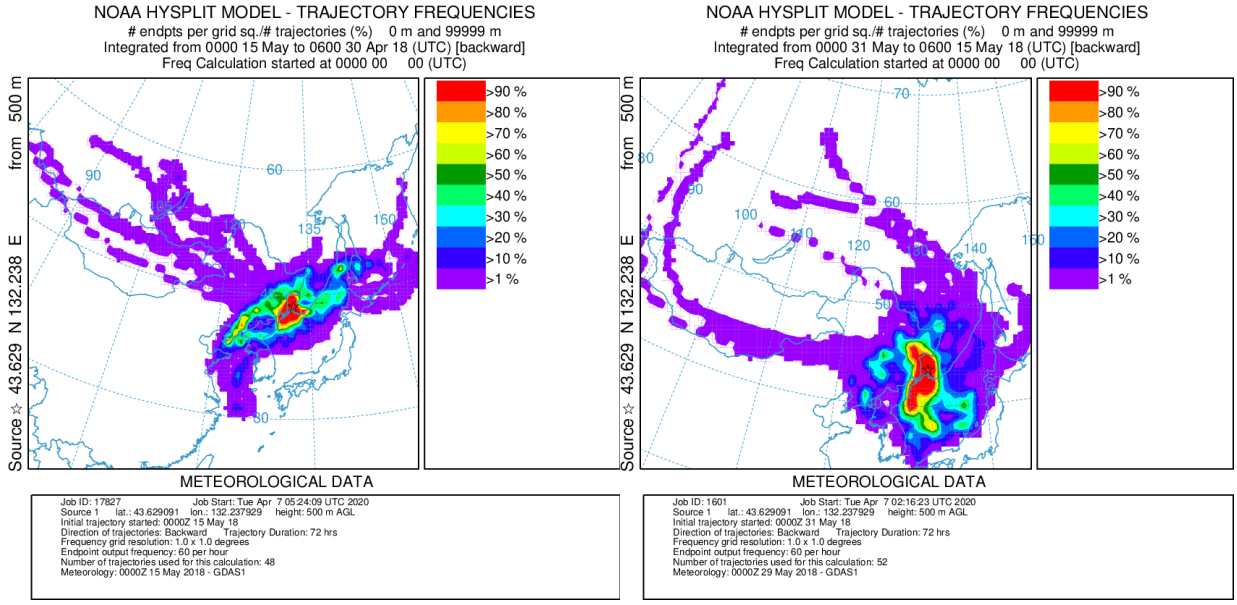
NOAA HYSPLIT MODEL - TRAJECTORY FREQUENCIES
endpts per grid sq./# trajectories (%) 0 m and 99999 m
Integrated from 0000 15 May to 0600 30 Apr 18 (UTC) [backward]
Freq Calculation started at 0000 00 00 (UTC)
Source ☆ 43.629 N 132.238 E from 500 m
>90 %
>80 %
>70 %
>60 %
>50 %
>40 %
>30 %
>20 %
>10 %
>1 %
METEOROLOGICAL DATA
Job ID: 17827 Job Start: Tue Apr 7 05:24:09 UTC 2020
Source 1 lat.: 43.629091 lon.: 132.237929 height: 500 m AGL
Initial trajectory started: 0000Z 15 May 18
Direction of trajectories: Backward Trajectory Duration: 72 hrs
Frequency grid resolution: 1.0 x 1.0 degrees
Endpoint output frequency: 60 per hour
Number of trajectories used for this calculation: 48
Meteorology: 0000Z 15 May 2018 - GDAS1

NOAA HYSPLIT MODEL - TRAJECTORY FREQUENCIES
endpts per grid sq./# trajectories (%) 0 m and 99999 m
Integrated from 0000 31 May to 0600 15 May 18 (UTC) [backward]
Freq Calculation started at 0000 00 00 (UTC)
Source ☆ 43.629 N 132.238 E from 500 m
>90 %
>80 %
>70 %
>60 %
>50 %
>40 %
>30 %
>20 %
>10 %
>1 %
METEOROLOGICAL DATA
Job ID: 1601 Job Start: Tue Apr 7 02:16:23 UTC 2020
Source 1 lat.: 43.629091 lon.: 132.237929 height: 500 m AGL
Initial trajectory started: 0000Z 31 May 18
Direction of trajectories: Backward Trajectory Duration: 72 hrs
Frequency grid resolution: 1.0 x 1.0 degrees
Endpoint output frequency: 60 per hour
Number of trajectories used for this calculation: 52
Meteorology: 0000Z 29 May 2018 - GDAS1

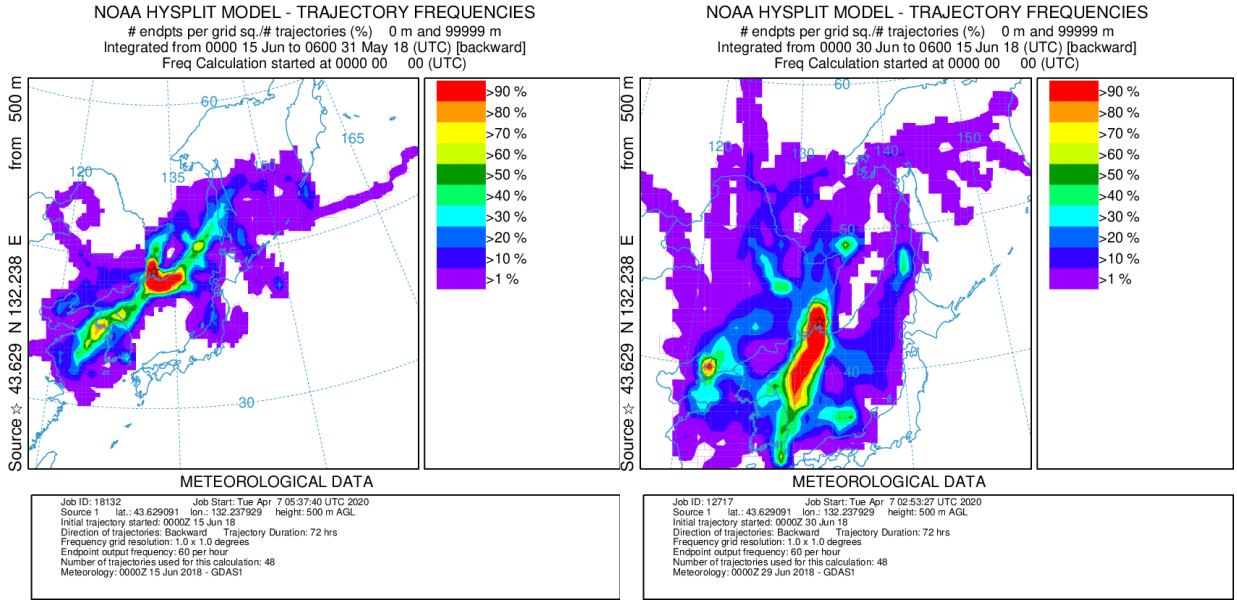
NOAA HYSPLIT MODEL - TRAJECTORY FREQUENCIES
endpts per grid sq./# trajectories (%) 0 m and 99999 m
Integrated from 0000 15 Jun to 0600 31 May 18 (UTC) [backward]
Freq Calculation started at 0000 00 00 (UTC)
Source ☆ 43.629 N 132.238 E from 500 m
>90 %
>80 %
>70 %
>60 %
>50 %
>40 %
>30 %
>20 %
>10 %
>1 %
METEOROLOGICAL DATA
Job ID: 18132 Job Start: Tue Apr 7 05:37:40 UTC 2020
Source 1 lat.: 43.629091 lon.: 132.237929 height: 500 m AGL
Initial trajectory started: 0000Z 15 Jun 18
Direction of trajectories: Backward Trajectory Duration: 72 hrs
Frequency grid resolution: 1.0 x 1.0 degrees
Endpoint output frequency: 60 per hour
Number of trajectories used for this calculation: 48
Meteorology: 0000Z 15 Jun 2018 - GDAS1

NOAA HYSPLIT MODEL - TRAJECTORY FREQUENCIES
endpts per grid sq./# trajectories (%) 0 m and 99999 m
Integrated from 0000 30 Jun to 0600 15 Jun 18 (UTC) [backward]
Freq Calculation started at 0000 00 00 (UTC)
Source ☆ 43.629 N 132.238 E from 500 m
>90 %
>80 %
>70 %
>60 %
>50 %
>40 %
>30 %
>20 %
>10 %
>1 %
METEOROLOGICAL DATA
Job ID: 12717 Job Start: Tue Apr 7 02:53:27 UTC 2020
Source 1 lat.: 43.629091 lon.: 132.237929 height: 500 m AGL
Initial trajectory started: 0000Z 30 Jun 18
Direction of trajectories: Backward Trajectory Duration: 72 hrs
Frequency grid resolution: 1.0 x 1.0 degrees
Endpoint output frequency: 60 per hour
Number of trajectories used for this calculation: 48
Meteorology: 0000Z 29 Jun 2018 - GDAS1

NOAA HYSPLIT MODEL - TRAJECTORY FREQUENCIES
endpts per grid sq./# trajectories (%) 0 m and 99999 m
Integrated from 0000 15 Jul to 0600 30 Jun 18 (UTC) [backward]
Freq Calculation started at 0000 00 00 (UTC)

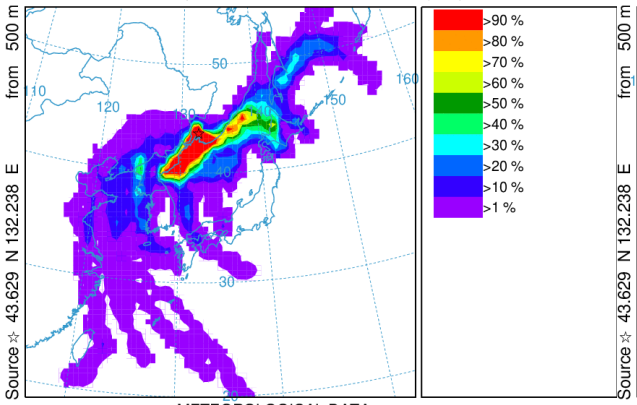

METEOROLOGICAL DATA

Job ID: 18309 Job Start: Tue Apr 7 05:44:55 UTC 2020
Source 1 lat.: 43.629091 lon.: 132.237929 height: 500 m AGL
Initial trajectory started: 0000Z 15 Jul 18
Direction of trajectories: Backward Trajectory Duration: 72 hrs
Frequency grid resolution: 1.0 x 1.0 degrees
Endpoint output frequency: 60 per hour
Number of trajectories used for this calculation: 48
Meteorology: 0000Z 15 Jul 2018 - GDAS1

NOAA HYSPLIT MODEL - TRAJECTORY FREQUENCIES
endpts per grid sq./# trajectories (%) 0 m and 99999 m
Integrated from 0000 31 Jul to 0600 15 Jul 18 (UTC) [backward]
Freq Calculation started at 0000 00 00 (UTC)

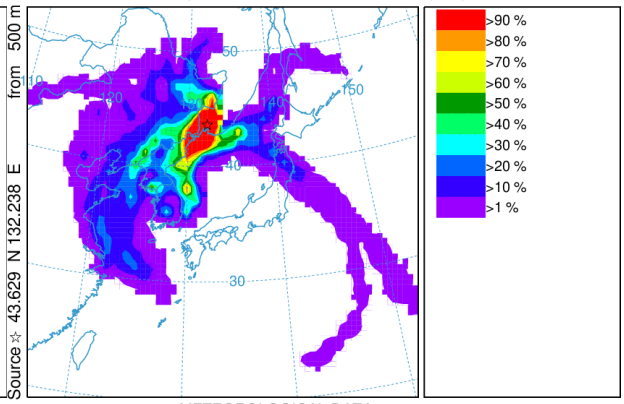

METEOROLOGICAL DATA

Job ID: 1373 Job Start: Tue Apr 7 02:11:20 UTC 2020
Source 1 lat.: 43.629091 lon.: 132.237929 height: 500 m AGL
Initial trajectory started: 0000Z 31 Jul 18
Direction of trajectories: Backward Trajectory Duration: 72 hrs
Frequency grid resolution: 1.0 x 1.0 degrees
Endpoint output frequency: 60 per hour
Number of trajectories used for this calculation: 52
Meteorology: 0000Z 29 Jul 2018 - GDAS1

NOAA HYSPLIT MODEL - TRAJECTORY FREQUENCIES
endpts per grid sq./# trajectories (%) 0 m and 99999 m
Integrated from 0000 15 Aug to 0600 31 Jul 18 (UTC) [backward]
Freq Calculation started at 0000 00 00 (UTC)

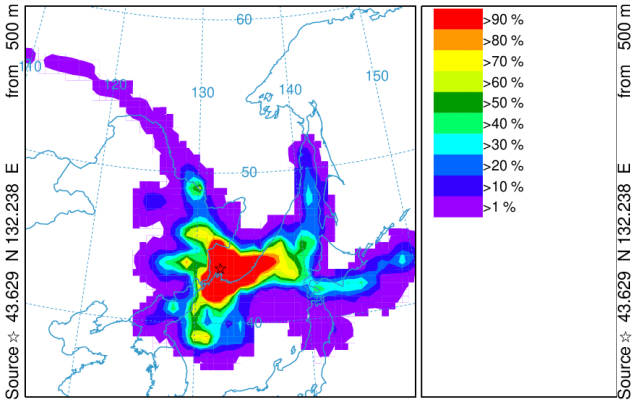

METEOROLOGICAL DATA

Job ID: 18508 Job Start: Tue Apr 7 05:51:53 UTC 2020
Source 1 lat.: 43.629091 lon.: 132.237929 height: 500 m AGL
Initial trajectory started: 0000Z 15 Aug 18
Direction of trajectories: Backward Trajectory Duration: 72 hrs
Frequency grid resolution: 1.0 x 1.0 degrees
Endpoint output frequency: 60 per hour
Number of trajectories used for this calculation: 48
Meteorology: 0000Z 15 Aug 2018 - GDAS1

NOAA HYSPLIT MODEL - TRAJECTORY FREQUENCIES
endpts per grid sq./# trajectories (%) 0 m and 99999 m
Integrated from 0000 31 Aug to 0600 15 Aug 18 (UTC) [backward]
Freq Calculation started at 0000 00 00 (UTC)

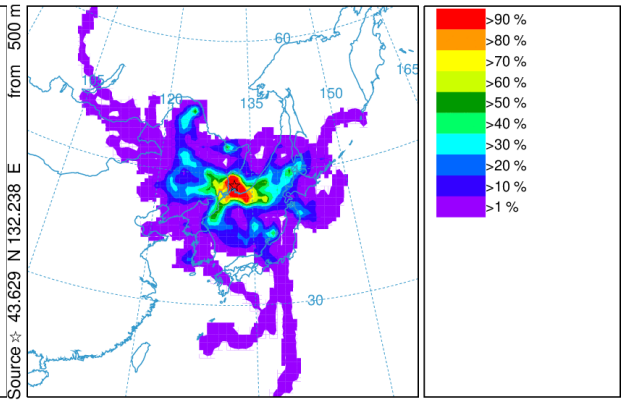

METEOROLOGICAL DATA

Job ID: 199960 Job Start: Tue Apr 7 02:04:14 UTC 2020
Source 1 lat.: 43.629091 lon.: 132.237929 height: 500 m AGL
Initial trajectory started: 0000Z 31 Aug 18
Direction of trajectories: Backward Trajectory Duration: 72 hrs
Frequency grid resolution: 1.0 x 1.0 degrees
Endpoint output frequency: 60 per hour
Number of trajectories used for this calculation: 52
Meteorology: 0000Z 29 Aug 2018 - GDAS1

NOAA HYSPLIT MODEL - TRAJECTORY FREQUENCIES
endpts per grid sq./# trajectories (%) 0 m and 99999 m
Integrated from 0000 15 Sep to 0600 31 Aug 18 (UTC) [backward]
Freq Calculation started at 0000 00 00 (UTC)

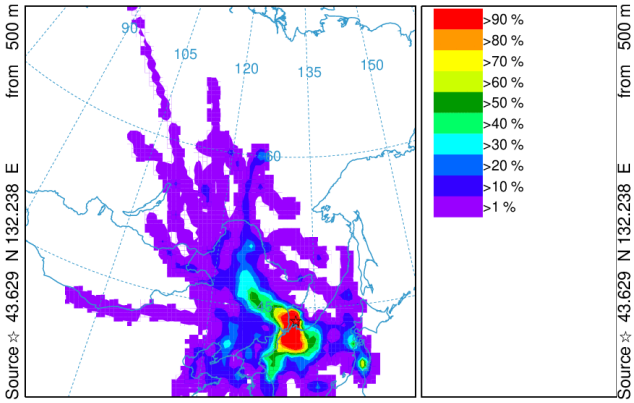

METEOROLOGICAL DATA

Job ID: 18690 Job Start: Tue Apr 7 05:59:27 UTC 2020
Source 1 lat.: 43.629091 lon.: 132.237929 height: 500 m AGL
Initial trajectory started: 0000Z 15 Sep 18
Direction of trajectories: Backward Trajectory Duration: 72 hrs
Frequency grid resolution: 1.0 x 1.0 degrees
Endpoint output frequency: 60 per hour
Number of trajectories used for this calculation: 48
Meteorology: 0000Z 15 Sep 2018 - GDAS1

NOAA HYSPLIT MODEL - TRAJECTORY FREQUENCIES
endpts per grid sq./# trajectories (%) 0 m and 99999 m
Integrated from 0000 30 Sep to 0600 15 Sep 18 (UTC) [backward]
Freq Calculation started at 0000 00 00 (UTC)

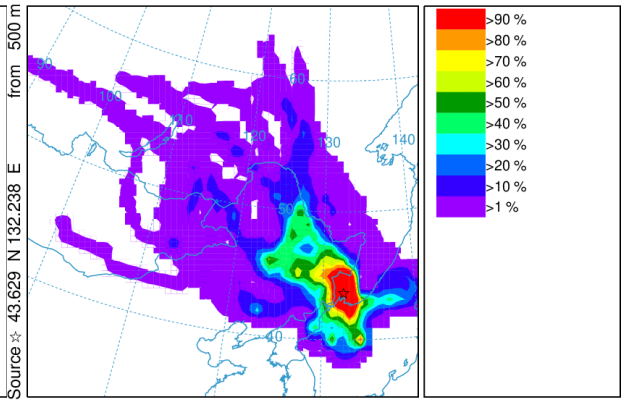

METEOROLOGICAL DATA

Job ID: 16287 Job Start: Tue Apr 7 04:24:55 UTC 2020
Source 1 lat.: 43.629091 lon.: 132.237929 height: 500 m AGL
Initial trajectory started: 0000Z 30 Sep 18
Direction of trajectories: Backward Trajectory Duration: 72 hrs
Frequency grid resolution: 1.0 x 1.0 degrees
Endpoint output frequency: 60 per hour
Number of trajectories used for this calculation: 48
Meteorology: 0000Z 29 Sep 2018 - GDAS1

NOAA HYSPLIT MODEL - TRAJECTORY FREQUENCIES
endpts per grid sq./# trajectories (%) 0 m and 99999 m
Integrated from 0000 15 Oct to 0600 30 Sep 18 (UTC) [backward]
Freq Calculation started at 0000 00 00 (UTC)

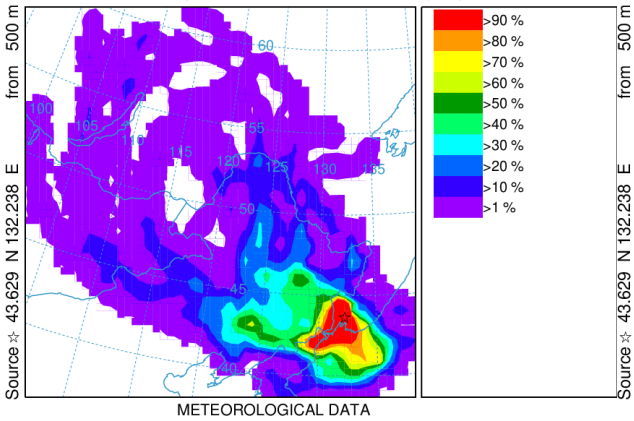

METEOROLOGICAL DATA

Job ID: 18875 Job Start: Tue Apr 7 06:06:33 UTC 2020
Source 1 lat.: 43.629091 lon.: 132.237929 height: 500 m AGL
Initial trajectory started: 0000Z 15 Oct 18
Direction of trajectories: Backward Trajectory Duration: 72 hrs
Frequency grid resolution: 1.0 x 1.0 degrees
Endpoint output frequency: 60 per hour
Number of trajectories used for this calculation: 48
Meteorology: 0000Z 15 Oct 2018 - GDAS1

NOAA HYSPLIT MODEL - TRAJECTORY FREQUENCIES
endpts per grid sq./# trajectories (%) 0 m and 99999 m
Integrated from 0000 31 Oct to 0600 15 Oct 18 (UTC) [backward]
Freq Calculation started at 0000 00 00 (UTC)

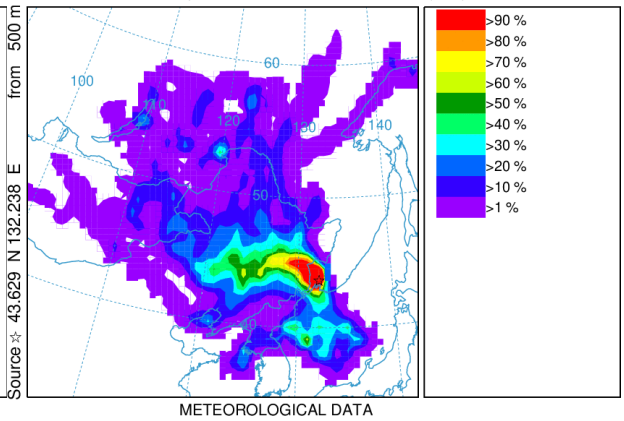

METEOROLOGICAL DATA

Job ID: 199382 Job Start: Tue Apr 7 01:52:34 UTC 2020
Source 1 lat.: 43.629091 lon.: 132.237929 height: 500 m AGL
Initial trajectory started: 0000Z 31 Oct 18
Direction of trajectories: Backward Trajectory Duration: 72 hrs
Frequency grid resolution: 1.0 x 1.0 degrees
Endpoint output frequency: 60 per hour
Number of trajectories used for this calculation: 52
Meteorology: 0000Z 29 Oct 2018 - GDAS1

NOAA HYSPLIT MODEL - TRAJECTORY FREQUENCIES
endpts per grid sq./# trajectories (%) 0 m and 99999 m
Integrated from 0000 15 Nov to 0600 31 Oct 18 (UTC) [backward]
Freq Calculation started at 0000 00 00 (UTC)

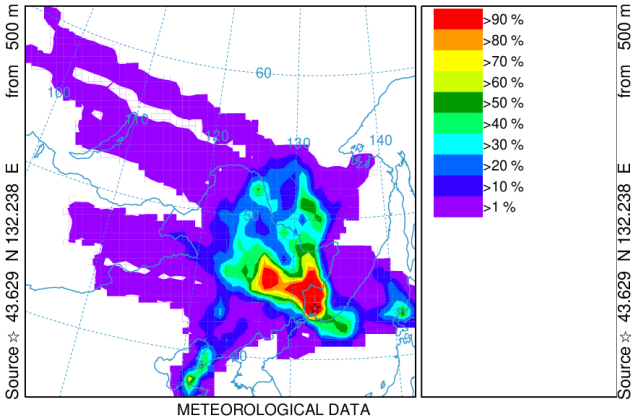

METEOROLOGICAL DATA

Job ID: 19043 Job Start: Tue Apr 7 06:14:00 UTC 2020
Source 1 lat.: 43.629091 lon.: 132.237929 height: 500 m AGL
Initial trajectory started: 0000Z 15 Nov 18
Direction of trajectories: Backward Trajectory Duration: 72 hrs
Frequency grid resolution: 1.0 x 1.0 degrees
Endpoint output frequency: 60 per hour
Number of trajectories used for this calculation: 48
Meteorology: 0000Z 15 Nov 2018 - GDAS1

NOAA HYSPLIT MODEL - TRAJECTORY FREQUENCIES
endpts per grid sq./# trajectories (%) 0 m and 99999 m
Integrated from 0000 30 Nov to 0600 15 Nov 18 (UTC) [backward]
Freq Calculation started at 0000 00 00 (UTC)

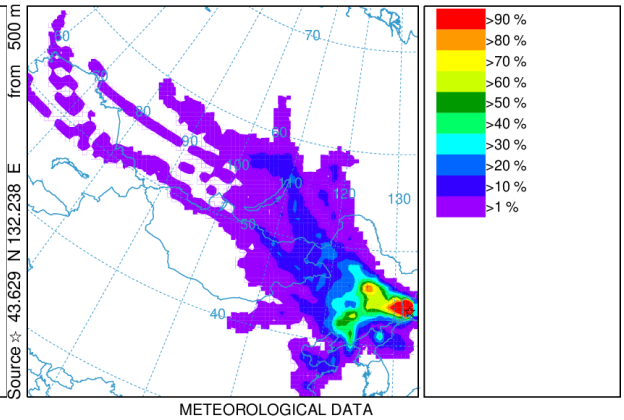

METEOROLOGICAL DATA

Job ID: 16456 Job Start: Tue Apr 7 04:30:16 UTC 2020
Source 1 lat.: 43.629091 lon.: 132.237929 height: 500 m AGL
Initial trajectory started: 0000Z 30 Nov 18
Direction of trajectories: Backward Trajectory Duration: 72 hrs
Frequency grid resolution: 1.0 x 1.0 degrees
Endpoint output frequency: 60 per hour
Number of trajectories used for this calculation: 48
Meteorology: 0000Z 29 Nov 2018 - GDAS1

NOAA HYSPLIT MODEL - TRAJECTORY FREQUENCIES
endpts per grid sq./# trajectories (%) 0 m and 99999 m
Integrated from 0000 15 Dec to 0600 30 Nov 18 (UTC) [backward]
Freq Calculation started at 0000 00 00 (UTC)

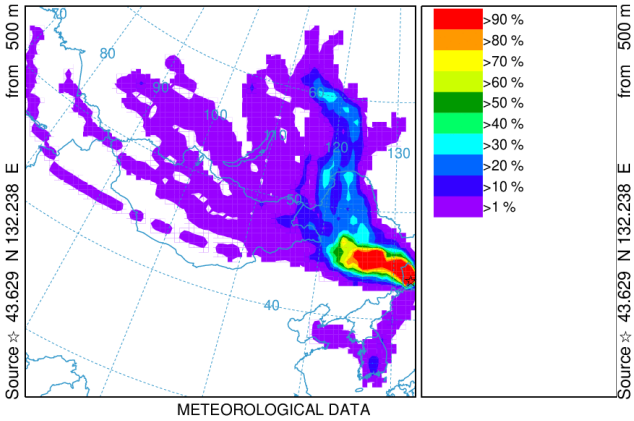

METEOROLOGICAL DATA

Job ID: 19175 Job Start: Tue Apr 7 06:22:45 UTC 2020
Source 1 lat.: 43.629091 lon.: 132.237929 height: 500 m AGL
Initial trajectory started: 0000Z 15 Dec 18
Direction of trajectories: Backward Trajectory Duration: 72 hrs
Frequency grid resolution: 1.0 x 1.0 degrees
Endpoint output frequency: 60 per hour
Number of trajectories used for this calculation: 48
Meteorology: 0000Z 15 Dec 2018 - GDAS1

NOAA HYSPLIT MODEL - TRAJECTORY FREQUENCIES
endpts per grid sq./# trajectories (%) 0 m and 99999 m
Integrated from 0000 31 Dec to 0600 15 Dec 18 (UTC) [backward]
Freq Calculation started at 0000 00 00 (UTC)

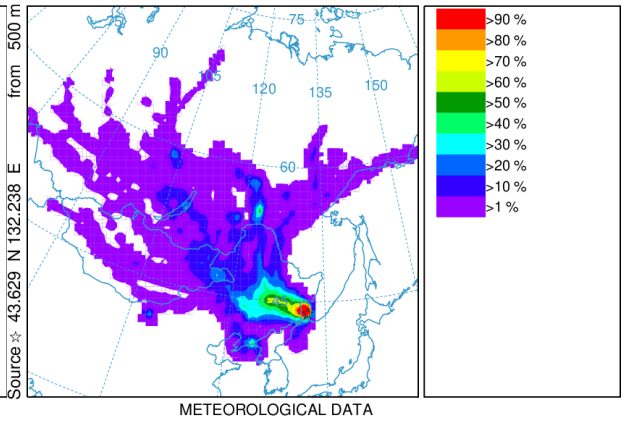

METEOROLOGICAL DATA

Job ID: 199757 Job Start: Tue Apr 7 01:59:41 UTC 2020
Source 1 lat.: 43.629091 lon.: 132.237929 height: 500 m AGL
Initial trajectory started: 0000Z 31 Dec 18
Direction of trajectories: Backward Trajectory Duration: 72 hrs
Frequency grid resolution: 1.0 x 1.0 degrees
Endpoint output frequency: 60 per hour
Number of trajectories used for this calculation: 52
Meteorology: 0000Z 29 Dec 2018 - GDAS1

Appendix 2. Results of L-Q equation calculations

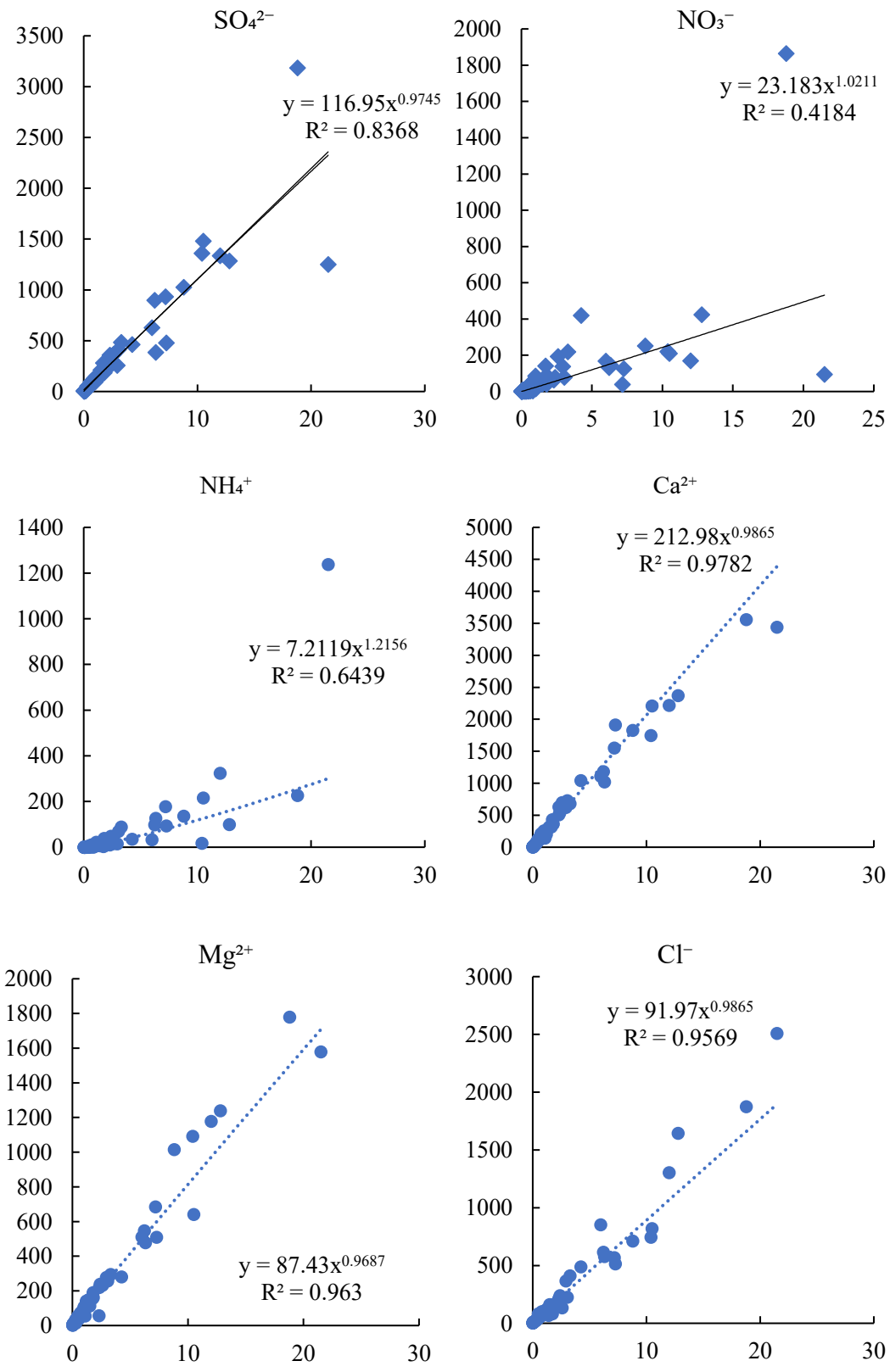

Appendix 3. 72-hours airmasses backward trajectories ending at KJK site at heights 100, 500, and 1000m in 2018 for every air sampling event calculated by HYSPLIT.

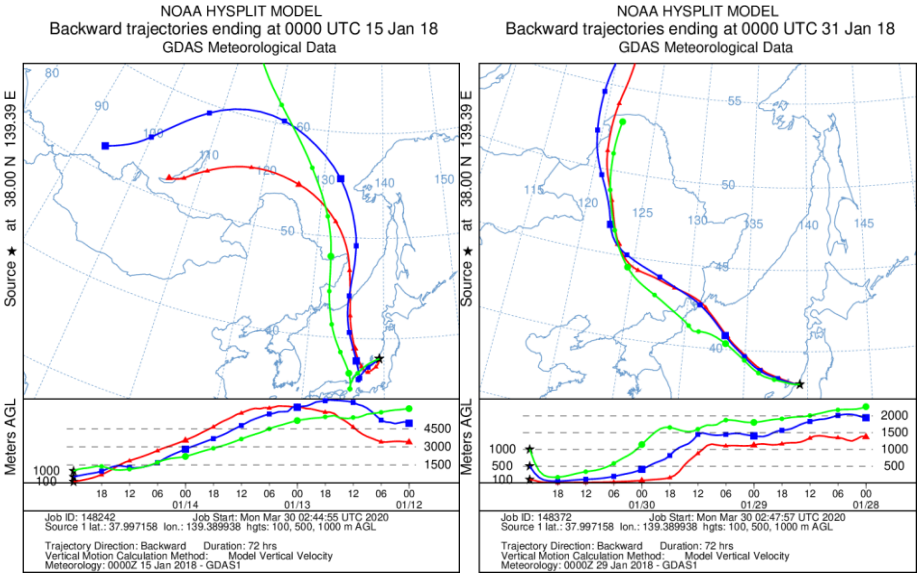

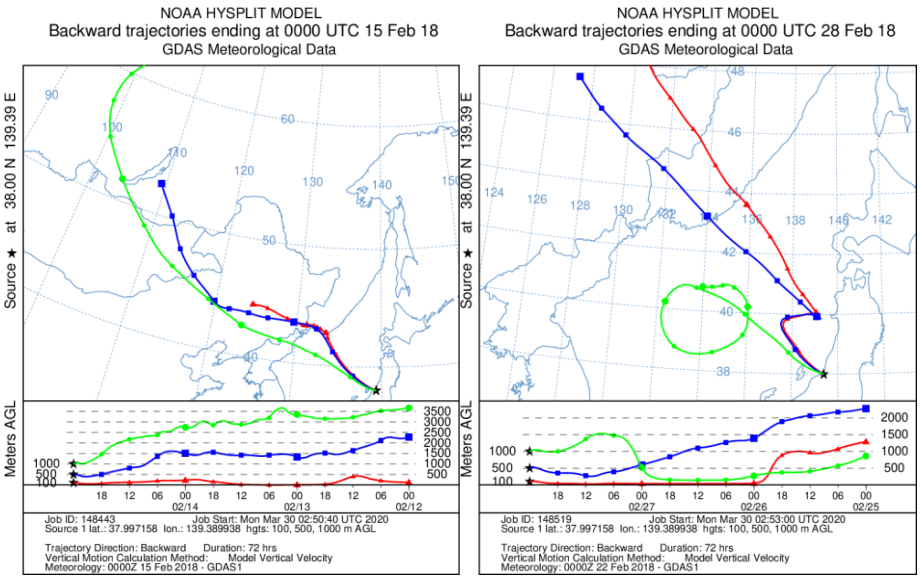

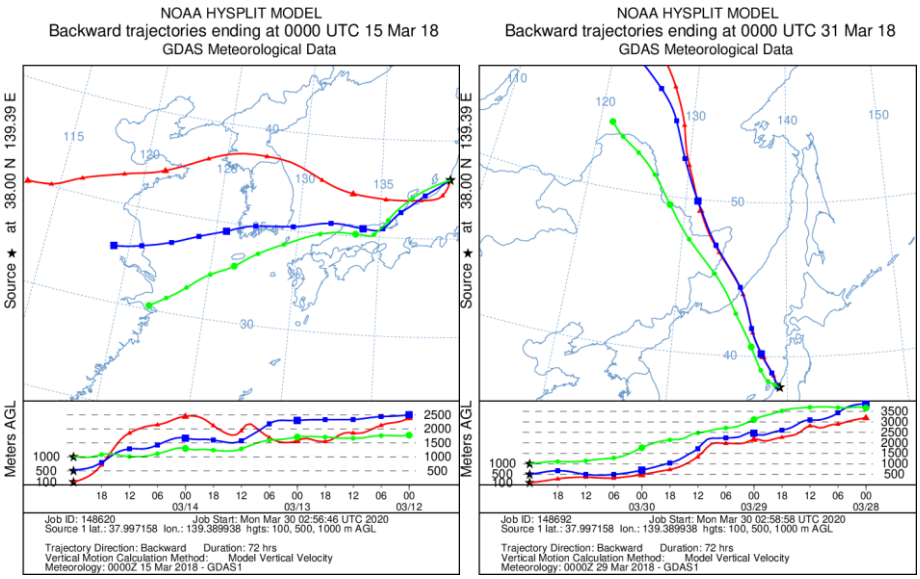

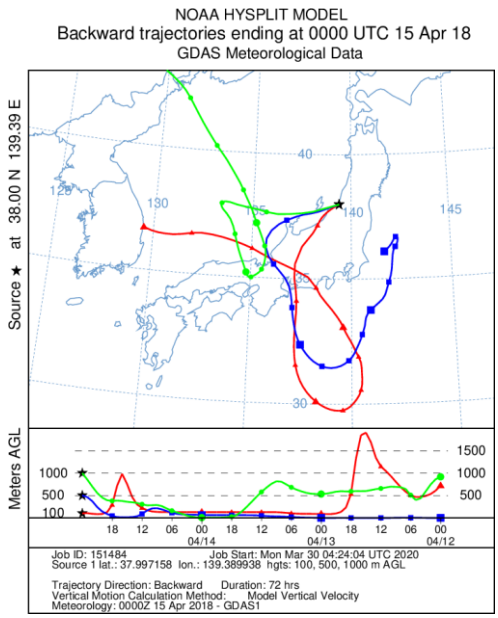
NOAA HYSPLIT MODEL
Backward trajectories ending at 0000 UTC 15 Apr 18
GDAS Meteorological Data
Source ★ at 38.00 N 139.39 E
Meters AGL
Job ID: 151484 Job Start: Mon Mar 30 04:24:04 UTC 2020
Source 1 lat.: 37.997158 lon.: 139.389938 hgts: 100, 500, 1000 m AGL
Trajectory Direction: Backward Duration: 72 hrs
Vertical Motion Calculation Method: Model Vertical Velocity
Meteorology: 0000Z 15 Apr 2018 - GDAS1

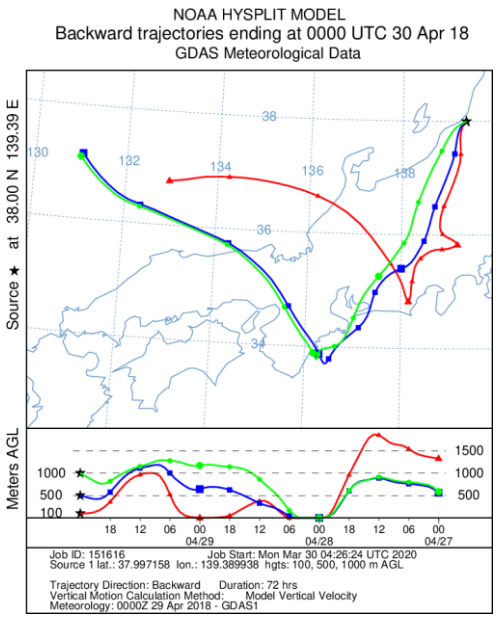
NOAA HYSPLIT MODEL
Backward trajectories ending at 0000 UTC 30 Apr 18
GDAS Meteorological Data
Source ★ at 38.00 N 139.39 E
Meters AGL
Job ID: 151616 Job Start: Mon Mar 30 04:26:24 UTC 2020
Source 1 lat.: 37.997158 lon.: 139.389938 hgts: 100, 500, 1000 m AGL
Trajectory Direction: Backward Duration: 72 hrs
Vertical Motion Calculation Method: Model Vertical Velocity
Meteorology: 0000Z 29 Apr 2018 - GDAS1

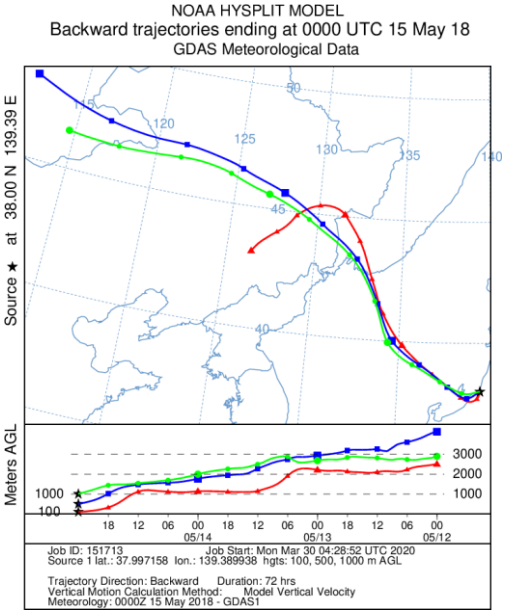
NOAA HYSPLIT MODEL
Backward trajectories ending at 0000 UTC 15 May 18
GDAS Meteorological Data
Source ★ at 38.00 N 139.39 E
Meters AGL
Job ID: 151713 Job Start: Mon Mar 30 04:28:52 UTC 2020
Source 1 lat.: 37.997158 lon.: 139.389938 hgts: 100, 500, 1000 m AGL
Trajectory Direction: Backward Duration: 72 hrs
Vertical Motion Calculation Method: Model Vertical Velocity
Meteorology: 0000Z 15 May 2018 - GDAS1

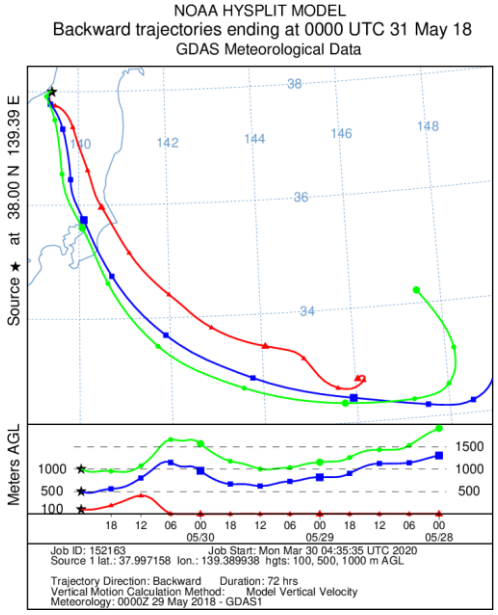
NOAA HYSPLIT MODEL
Backward trajectories ending at 0000 UTC 31 May 18
GDAS Meteorological Data
Source ★ at 38.00 N 139.39 E
Meters AGL
Job ID: 152163 Job Start: Mon Mar 30 04:35:35 UTC 2020
Source 1 lat.: 37.997158 lon.: 139.389938 hgts: 100, 500, 1000 m AGL
Trajectory Direction: Backward Duration: 72 hrs
Vertical Motion Calculation Method: Model Vertical Velocity
Meteorology: 0000Z 29 May 2018 - GDAS1

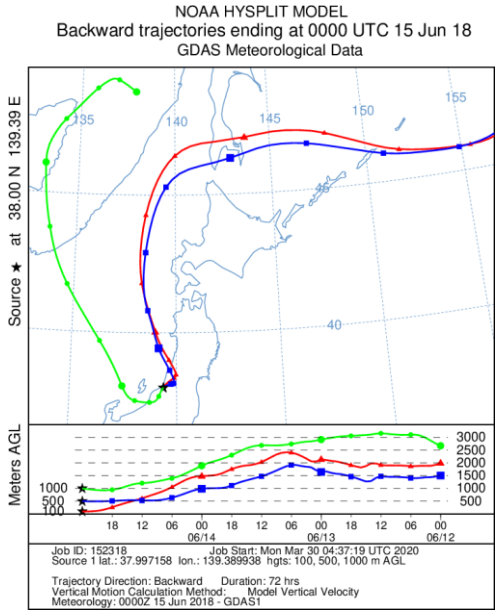
NOAA HYSPLIT MODEL
Backward trajectories ending at 0000 UTC 15 Jun 18
GDAS Meteorological Data
Source ★ at 38.00 N 139.39 E
Meters AGL
Job ID: 152318 Job Start: Mon Mar 30 04:37:19 UTC 2020
Source 1 lat.: 37.997158 lon.: 139.389938 hgts: 100, 500, 1000 m AGL
Trajectory Direction: Backward Duration: 72 hrs
Vertical Motion Calculation Method: Model Vertical Velocity
Meteorology: 0000Z 15 Jun 2018 - GDAS1

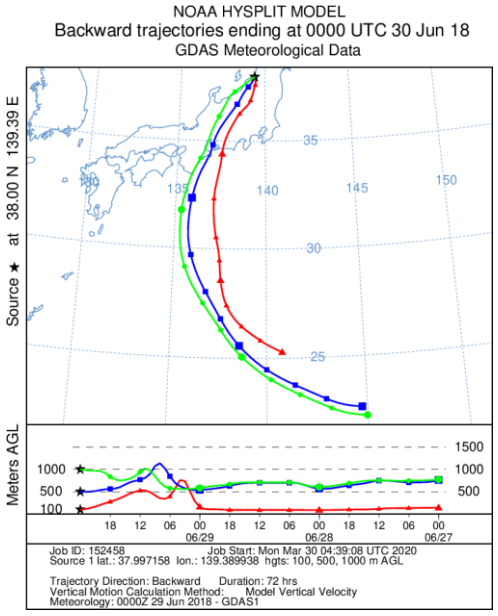
NOAA HYSPLIT MODEL
Backward trajectories ending at 0000 UTC 30 Jun 18
GDAS Meteorological Data
Source ★ at 38.00 N 139.39 E
Meters AGL
Job ID: 152458 Job Start: Mon Mar 30 04:39:08 UTC 2020
Source 1 lat.: 37.997158 lon.: 139.389938 hgts: 100, 500, 1000 m AGL
Trajectory Direction: Backward Duration: 72 hrs
Vertical Motion Calculation Method: Model Vertical Velocity
Meteorology: 0000Z 29 Jun 2018 - GDAS1

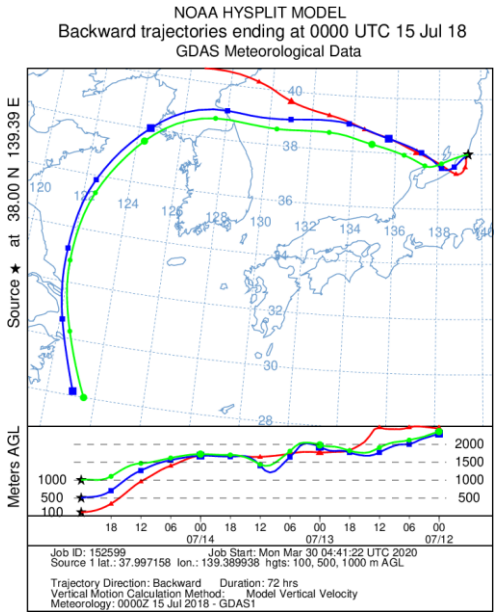
NOAA HYSPLIT MODEL
Backward trajectories ending at 0000 UTC 15 Jul 18
GDAS Meteorological Data
Source ★ at 38.00 N 139.39 E
Meters AGL
Job ID: 152599 Job Start: Mon Mar 30 04:41:22 UTC 2020
Source 1 lat.: 37.997158 lon.: 139.389938 hgts: 100, 500, 1000 m AGL
Trajectory Direction: Backward Duration: 72 hrs
Vertical Motion Calculation Method: Model Vertical Velocity
Meteorology: 0000Z 15 Jul 2018 - GDAS1

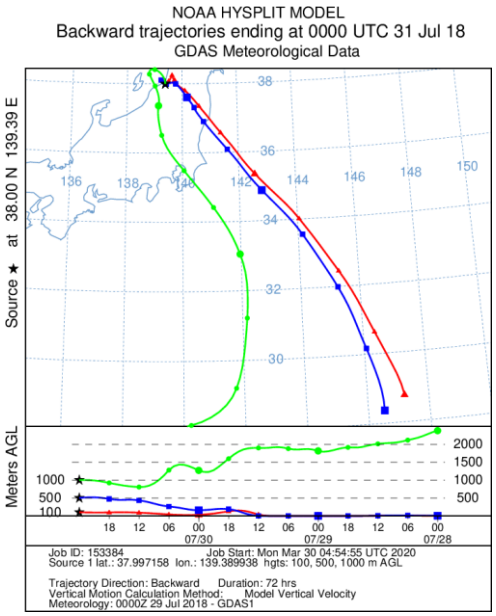
NOAA HYSPLIT MODEL
Backward trajectories ending at 0000 UTC 31 Jul 18
GDAS Meteorological Data
Source ★ at 38.00 N 139.39 E
Meters AGL
Job ID: 153384 Job Start: Mon Mar 30 04:54:55 UTC 2020
Source 1 lat.: 37.997158 lon.: 139.389938 hgts: 100, 500, 1000 m AGL
Trajectory Direction: Backward Duration: 72 hrs
Vertical Motion Calculation Method: Model Vertical Velocity
Meteorology: 0000Z 29 Jul 2018 - GDAS1

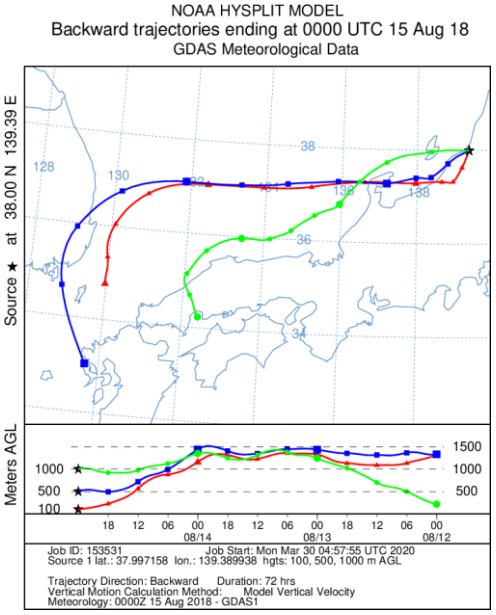
NOAA HYSPLIT MODEL
Backward trajectories ending at 0000 UTC 15 Aug 18
GDAS Meteorological Data
Source ★ at 38.00 N 139.39 E
Meters AGL
Job ID: 153531 Job Start: Mon Mar 30 04:57:55 UTC 2020
Source 1 lat.: 37.997158 lon.: 139.389938 hgts: 100, 500, 1000 m AGL
Trajectory Direction: Backward Duration: 72 hrs
Vertical Motion Calculation Method: Model Vertical Velocity
Meteorology: 0000Z 15 Aug 2018 - GDAS1

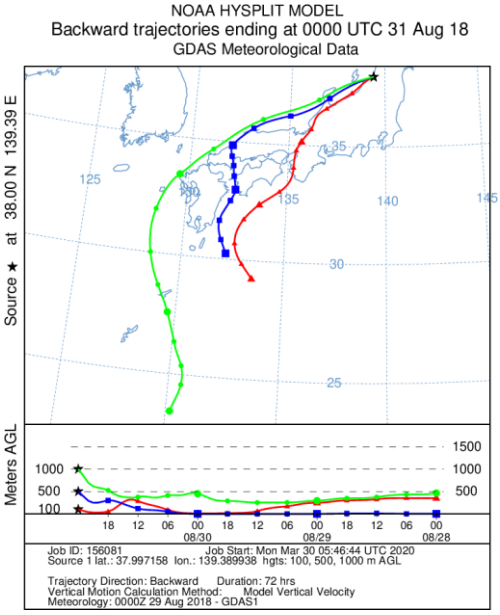
NOAA HYSPLIT MODEL
Backward trajectories ending at 0000 UTC 31 Aug 18
GDAS Meteorological Data
Source ★ at 38.00 N 139.39 E
Meters AGL
Job ID: 156081 Job Start: Mon Mar 30 05:46:44 UTC 2020
Source 1 lat.: 37.997158 lon.: 139.389938 hgts: 100, 500, 1000 m AGL
Trajectory Direction: Backward Duration: 72 hrs
Vertical Motion Calculation Method: Model Vertical Velocity
Meteorology: 0000Z 29 Aug 2018 - GDAS1

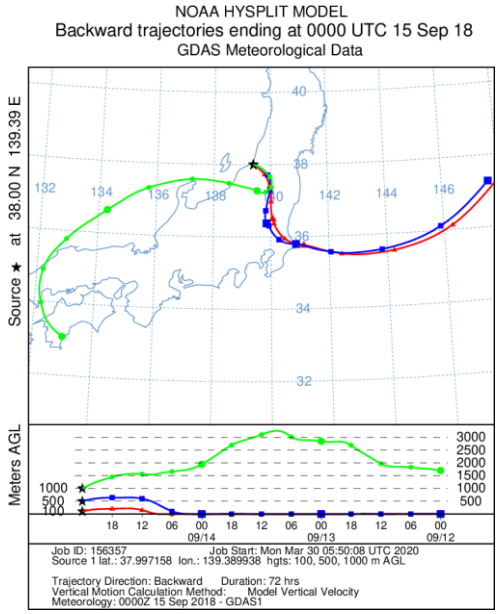
NOAA HYSPLIT MODEL
Backward trajectories ending at 0000 UTC 15 Sep 18
GDAS Meteorological Data
Source ★ at 38.00 N 139.39 E
Meters AGL
Job ID: 156357 Job Start: Mon Mar 30 05:50:08 UTC 2020
Source 1 lat.: 37.997158 lon.: 139.389938 hgts: 100, 500, 1000 m AGL
Trajectory Direction: Backward Duration: 72 hrs
Vertical Motion Calculation Method: Model Vertical Velocity
Meteorology: 0000Z 15 Sep 2018 - GDAS1

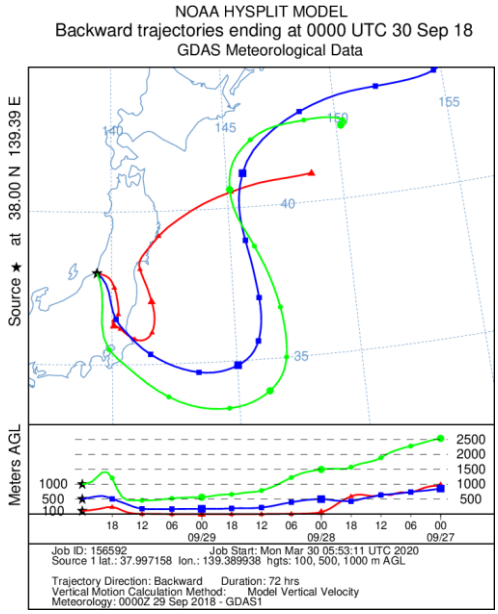
NOAA HYSPLIT MODEL
Backward trajectories ending at 0000 UTC 30 Sep 18
GDAS Meteorological Data
Source ★ at 38.00 N 139.39 E
Meters AGL
Job ID: 156592 Job Start: Mon Mar 30 05:53:11 UTC 2020
Source 1 lat.: 37.997158 lon.: 139.389938 hgts: 100, 500, 1000 m AGL
Trajectory Direction: Backward Duration: 72 hrs
Vertical Motion Calculation Method: Model Vertical Velocity
Meteorology: 0000Z 29 Sep 2018 - GDAS1

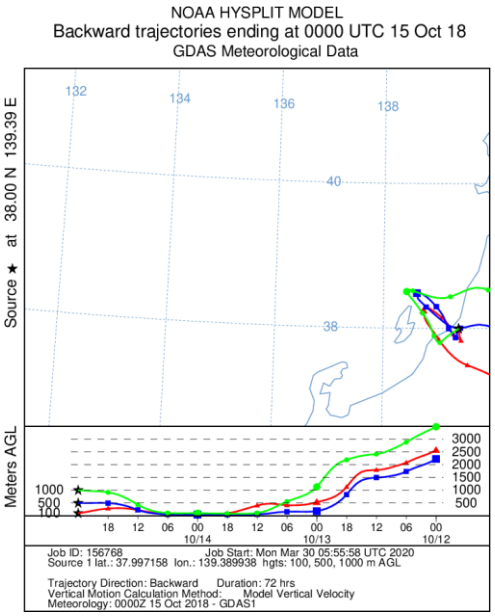
NOAA HYSPLIT MODEL
Backward trajectories ending at 0000 UTC 15 Oct 18
GDAS Meteorological Data
Source ★ at 38.00 N 139.39 E
Meters AGL
Job ID: 156768 Job Start: Mon Mar 30 05:55:58 UTC 2020
Source 1 lat.: 37.997158 lon.: 139.389938 hgts: 100, 500, 1000 m AGL
Trajectory Direction: Backward Duration: 72 hrs
Vertical Motion Calculation Method: Model Vertical Velocity
Meteorology: 0000Z 15 Oct 2018 - GDAS1

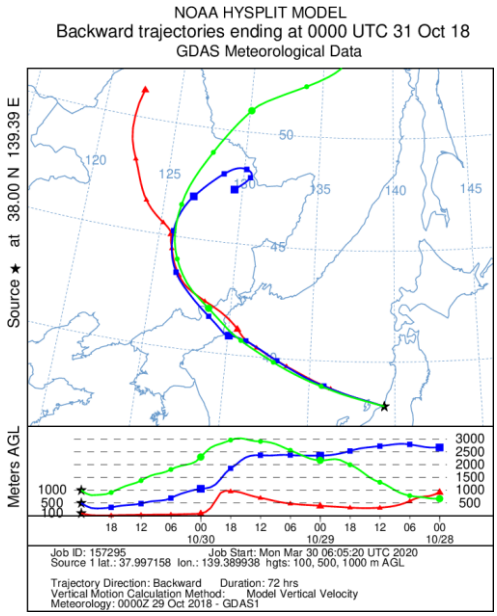
NOAA HYSPLIT MODEL
Backward trajectories ending at 0000 UTC 31 Oct 18
GDAS Meteorological Data
Source ★ at 38.00 N 139.39 E
Meters AGL
Job ID: 157295 Job Start: Mon Mar 30 06:05:20 UTC 2020
Source 1 lat.: 37.997158 lon.: 139.389938 hgts: 100, 500, 1000 m AGL
Trajectory Direction: Backward Duration: 72 hrs
Vertical Motion Calculation Method: Model Vertical Velocity
Meteorology: 0000Z 29 Oct 2018 - GDAS1

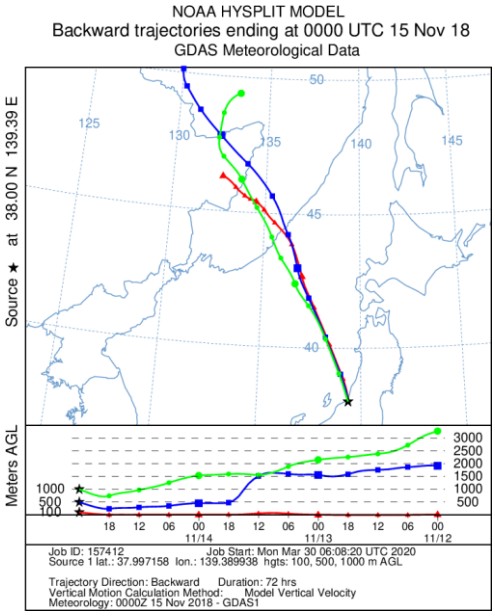
NOAA HYSPLIT MODEL
Backward trajectories ending at 0000 UTC 15 Nov 18
GDAS Meteorological Data
Source ★ at 38.00 N 139.39 E
Meters AGL
Job ID: 157412 Job Start: Mon Mar 30 06:08:20 UTC 2020
Source 1 lat.: 37.997158 lon.: 139.389938 hgts: 100, 500, 1000 m AGL
Trajectory Direction: Backward Duration: 72 hrs
Vertical Motion Calculation Method: Model Vertical Velocity
Meteorology: 0000Z 15 Nov 2018 - GDAS1

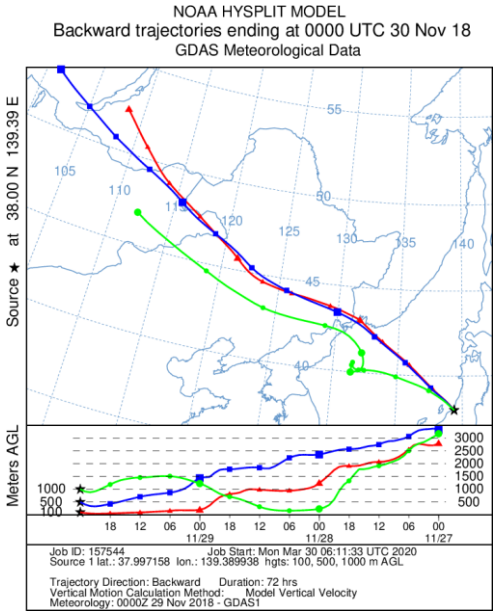
NOAA HYSPLIT MODEL
Backward trajectories ending at 0000 UTC 30 Nov 18
GDAS Meteorological Data
Source ★ at 38.00 N 139.39 E
Meters AGL
Job ID: 157544 Job Start: Mon Mar 30 06:11:33 UTC 2020
Source 1 lat.: 37.997158 lon.: 139.389938 hgts: 100, 500, 1000 m AGL
Trajectory Direction: Backward Duration: 72 hrs
Vertical Motion Calculation Method: Model Vertical Velocity
Meteorology: 0000Z 29 Nov 2018 - GDAS1

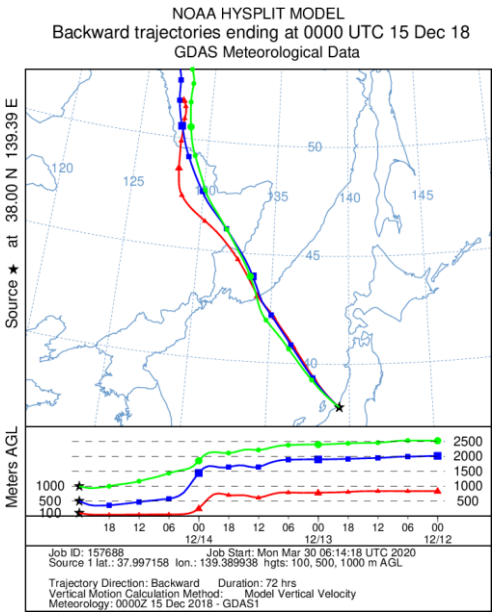
NOAA HYSPLIT MODEL
Backward trajectories ending at 0000 UTC 15 Dec 18
GDAS Meteorological Data
Source ★ at 38.00 N 139.39 E
Meters AGL
Job ID: 157688 Job Start: Mon Mar 30 06:14:18 UTC 2020
Source 1 lat.: 37.997158 lon.: 139.389938 hgts: 100, 500, 1000 m AGL
Trajectory Direction: Backward Duration: 72 hrs
Vertical Motion Calculation Method: Model Vertical Velocity
Meteorology: 0000Z 15 Dec 2018 - GDAS1

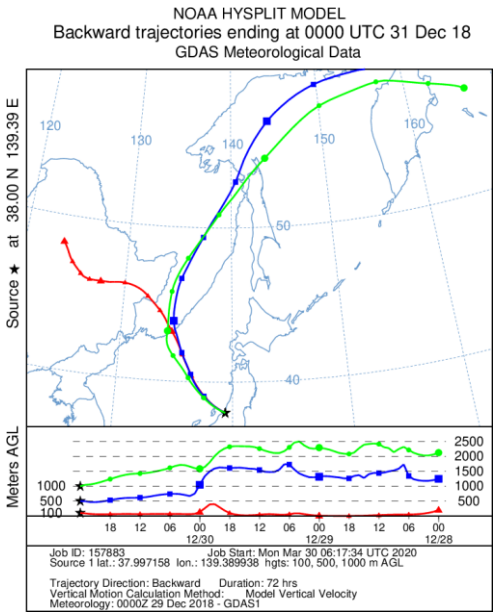
NOAA HYSPLIT MODEL
Backward trajectories ending at 0000 UTC 31 Dec 18
GDAS Meteorological Data
Source ★ at 38.00 N 139.39 E
Meters AGL
Job ID: 157883 Job Start: Mon Mar 30 06:17:34 UTC 2020
Source 1 lat.: 37.997158 lon.: 139.389938 hgts: 100, 500, 1000 m AGL
Trajectory Direction: Backward Duration: 72 hrs
Vertical Motion Calculation Method: Model Vertical Velocity
Meteorology: 0000Z 29 Dec 2018 - GDAS1

References

Aber, J. D., Goodale, C. L., Ollinger, S. V., Smith, M.-L., Magill, A. H., Martin, M. E., Hallett, R. A., & Stoddard, J. L. (2003). Is Nitrogen Deposition Altering the Nitrogen Status of Northeastern Forests? *BioScience*, *53*(4), 375–389. https://doi.org/10.1641/0006-3568(2003)053[0375:INDATN]2.0.CO;2

Baba, M., & Okazaki, M. (1998). Acidification in nitrogen-saturated forested catchment. *Soil Science and Plant Nutrition*, *44*(4), 513–525. https://doi.org/10.1080/00380768.1998.10414475

Berndt, T., Stratmann, F., Brasel, S., Heintzenberg, J., Laaksonen, A., & Kulmala, M. (2008). SO2 oxidation products other than H2SO4 as a trigger of new particle formation. Part 1: Laboratory investigations. *Atmos. Chem. Phys.*, 10.

Bhatti, N., Streets, D. G., & Foell, W. K. (1992). Acid rain in Asia. *Environmental Management*, *16*(4), 541–562. https://doi.org/10.1007/BF02394130

Bogatov, V. V., Fedorovskiy, A. S., & Nikulina, T. V. (2013). Role of hydrological factors in species diversity of algal communities: A case study of the Komarovka River, Primorye, Russia. *Russian Journal of Ecology*, *44*(6), 468–474. https://doi.org/10.1134/S1067413613060039

Bouwman, A. F., Van Vuuren, D. P., Derwent, R. G., & Posch, M. (2002). A Global Analysis of Acidification and Eutrophication of Terrestrial Ecosystems. *Water, Air, and Soil Pollution*, *141*(1), 349–382. https://doi.org/10.1023/A:1021398008726

Carriera, J. A., Lajtha, K., & Niell, F. X. (1997). Phosphorus transformations along a soil/vegetation series of fire-prone, dolomitic, semi-arid shrublands of southern

Spain Soil P and Mediterranean shrubland dynamic. *Biogeochemistry*, *39*(1), 87–120. https://doi.org/10.1023/A:1005871404474

Driscoll, C. T., Lambert, K. F., & Chen, L. (2007). Acidic Deposition: Sources and Ecological Effects. In G. R. Visgilio & D. M. Whitelaw (Eds.), *Acid in the Environment: Lessons Learned and Future Prospects* (pp. 27–58). Springer US. https://doi.org/10.1007/978-0-387-37562-5_3

Duan, L., Ma, X., Larssen, T., Mulder, J., & Hao, J. (2011). Response of Surface Water Acidification in Upper Yangtze River to SO_2 Emissions Abatement in China. *Environmental Science & Technology*, *45*(8), 3275–3281. https://doi.org/10.1021/es1038672

Duan, L., Yu, Q., Zhang, Q., Wang, Z., Pan, Y., Larssen, T., Tang, J., & Mulder, J. (2016). Acid deposition in Asia: Emissions, deposition, and ecosystem effects. *Atmospheric Environment*, *146*, 55–69. https://doi.org/10.1016/j.atmosenv.2016.07.018

EANET. (2007). *Data report 2006* (p. 289). Network Center for EANET. https://monitoring.eanet.asia/document/public/index

EANET. (2010a). *Technical Manual for Wet Deposition Monitoring in East Asia—2010*. Network Center for EANET. https://www.eanet.asia/publications/

EANET. (2010b). *Technical Manual on Dry Deposition Flux Estimation in East Asia*. Network Center for EANET. https://www.eanet.asia/publications/

EANET. (2014). *Data report 2013* (p. 302). Network Center for EANET. https://monitoring.eanet.asia/document/public/index

EANET. (2016a). *The third Periodic Report on the State of Acid Deposition in East Asia. Part I. Regional Assessment* (p. 268). https://www.eanet.asia/publications/

EANET. (2016b). *The third Periodic Report on the State of Acid Deposition in East Asia. Part II. National Assessments*. https://www.eanet.asia/publications/

EANET. (2021). *Data report 2020* (p. 334). Network Center for EANET. https://monitoring.eanet.asia/document/public/index

EANET. (2022) *EANET Data on the Acid Deposition in the East Asian Region.* Network Center for EANET, https://monitoring.eanet.asia/document/public/index. Accessed 10 March 2022

Engardt, M., Simpson, D., Schwikowski, M., & Granat, L. (2017). Deposition of sulphur and nitrogen in Europe 1900–2050. Model calculations and comparison to historical observations. *Tellus B: Chemical and Physical Meteorology*, *69*(1), 1328945. https://doi.org/10.1080/16000889.2017.1328945

Fang, Y., Gundersen, P., Vogt, R. D., Koba, K., Chen, F., Chen, X. Y., & Yoh, M. (2011). Atmospheric deposition and leaching of nitrogen in Chinese forest ecosystems. *Journal of Forest Research*, *16*(5), 341–350. https://doi.org/10.1007/s10310-011-0267-4

Finlayson-Pitts, B. J., & Pitts, J. N. (2000). CHAPTER 1—Overview of the Chemistry of Polluted and Remote Atmospheres. In B. J. Finlayson-Pitts & J. N. Pitts (Eds.), *Chemistry of the Upper and Lower Atmosphere* (pp. 1–14). Academic Press. https://doi.org/10.1016/B978-012257060-5/50003-4

Garmo, Ø. A., Skjelkvåle, B. L., de Wit, H. A., Colombo, L., Curtis, C., Fölster, J., Hoffmann, A., Hruška, J., Høgåsen, T., Jeffries, D. S., Keller, W. B., Krám, P.,

Majer, V., Monteith, D. T., Paterson, A. M., Rogora, M., Rzychon, D., Steingruber, S., Stoddard, J. L., … Worsztynowicz, A. (2014). Trends in Surface Water Chemistry in Acidified Areas in Europe and North America from 1990 to 2008. *Water, Air, & Soil Pollution*, *225*(3), 1880. https://doi.org/10.1007/s11270-014-1880-6

Gorham, E. (1992). Atmospheric Deposition to Lakes and Its Ecological Effects: A Retrospective and Prospective View of Research. *Japanese Journal of Limnology RIZAAU*, *53*(3), 231–248.

Houle, D., Couture, S., & Gagnon, C. (2010). Relative role of decreasing precipitation sulfate and climate on recent lake recovery: LAKE RECOVERY-CLIMATE AND ACID RAIN. *Global Biogeochemical Cycles*, *24*(4), n/a-n/a. https://doi.org/10.1029/2009GB003757

Ide, J., Nagafuchi, O., Chiwa, M., Kume, A., Otsuki, K., & Ogawa, S. (2007). Effects of discharge level on the load of dissolved and particulate components of stream nitrogen and phosphorus from a small afforested watershed of Japanese cypress (*Chamaecyparis obtusa*). *Journal of Forest Research*, *12*(1), 45–56. https://doi.org/10.1007/s10310-006-0250-7

Inomata, Y., Ohizumi, T., Saito, T., Morohashi, M., Yamashita, N., Takahashi, M., Sase, H., Takahashi, K., Kaneyasu, N., Fujihara, M., Iwasaki, A., Nakagomi, K., Shiroma, T., & Yamaguchi, T. (2019). Estimating transboundary transported anthropogenic sulfate deposition in Japan using the sulfur isotopic ratio. *Science of The Total Environment*, *691*, 779–788. https://doi.org/10.1016/j.scitotenv.2019.07.004

Johnson, J., Graf Pannatier, E., Carnicelli, S., Cecchini, G., Clarke, N., Cools, N., Hansen, K., Meesenburg, H., Nieminen, T. M., Pihl-Karlsson, G., Titeux, H., Vanguelova, E., Verstraeten, A., Vesterdal, L., Waldner, P., & Jonard, M. (2018). The response of soil solution chemistry in European forests to decreasing acid deposition. *Global Change Biology*, *24*(8), 3603–3619. https://doi.org/10.1111/gcb.14156

Kawase, H., Yamazaki, T., Sugimoto, S., Sasai, T., Ito, R., Hamada, T., Kuribayashi, M., Fujita, M., Murata, A., Nosaka, M., & Sasaki, H. (2020). Changes in extremely heavy and light snow-cover winters due to global warming over high mountainous areas in central Japan. *Progress in Earth and Planetary Science*, *7*(1), 10. https://doi.org/10.1186/s40645-020-0322-x

Kobayashi, R., Sumarriani, Y., Yamashita, N., Ohta, T., Matsubara, H., Yagoh, H., Nakata, M., & Sase, H. (2013). Seasonal variation of water chemistry and sulfur budget in an acid-sensitive river along the Sea of Japan. *Limnology*, *14*(2), 195–209. https://doi.org/10.1007/s10201-012-0396-2

Kurokawa, J., & Ohara, T. (2020). Long-term historical trends in air pollutant emissions in Asia: Regional Emission inventory in ASia (REAS) version 3. *Atmospheric Chemistry and Physics*, *20*(21), 12761–12793. https://doi.org/10.5194/acp-20-12761-2020

Likens, G. E., & Bormann, F. H. (1995). Chemistry. In G. E. Likens & F. H. Bormann (Eds.), *Biogeochemistry of a Forested Ecosystem* (pp. 31–72). Springer. https://doi.org/10.1007/978-1-4612-4232-1_3

Lupakov, S. Yu. (2021). Estimation of the runoff elasticity of the rivers in the eastern part of the Amur River basin. *Geosystems of Transition Zones*, *5*(2), 179–188. https://doi.org/10.30730/gtrz.2021.5.2.179-188

Matsubara, H., Morimoto, S., Sase, H., Ohizumi, T., Sumida, H., Nakata, M., & Ueda, H. (2009). Long-Term Declining Trends in River Water pH in Central Japan. *Water, Air, and Soil Pollution*, *200*(1), 253–265. https://doi.org/10.1007/s11270-008-9909-3

Ministry of Natural Resources and Environment of the Russian Federation. (2020). *State Report On the State and Protection of the Environment of the Russian Federation in 2019*. https://www.mnr.gov.ru/docs/gosudarstvennye_doklady/

Mitchell, M. J., Driscoll, C. T., McHale, P. J., Roy, K. M., & Dong, Z. (2013). Lake/watershed sulfur budgets and their response to decreases in atmospheric sulfur deposition: Watershed and climate controls: REGULATION OF SULFUR BUDGETS OF FORESTED LAKE/WATERSHEDS. *Hydrological Processes*, *27*(5), 710–720. https://doi.org/10.1002/hyp.9670

Mitchell, M. J., & Likens, G. E. (2011). Watershed Sulfur Biogeochemistry: Shift from Atmospheric Deposition Dominance to Climatic Regulation. *Environmental Science & Technology*, *45*(12), 5267–5271. https://doi.org/10.1021/es200844n

Nakahara, O., Takahashi, M., Sase, H., Yamada, T., Matsuda, K., Ohizumi, T., Fukuhara, H., Inoue, T., Takahashi, A., Kobayashi, H., Hatano, R., & Hakamata, T. (2010). Soil and stream water acidification in a forested catchment in central Japan. *Biogeochemistry*, *97*(2–3), 141–158. https://doi.org/10.1007/s10533-009-9362-4

Novák, M., Kirchner, J. W., Groscheová, H., Havel, M., Černý, J., Krejčí, R., & Buzek, F. (2000). Sulfur isotope dynamics in two central european watersheds affected by high atmospheric deposition of SOx. *Geochimica et Cosmochimica Acta*, *64*(3), 367–383. https://doi.org/10.1016/S0016-7037(99)00298-7

Ohte, N., Mitchell, M. J., Shibata, H., Tokuchi, N., Toda, H., & Iwatsubo, G. (2001). Comparative Evaluation on Nitrogen Saturation of Forest Catchments in Japan and Northeastern United States. *Water, Air, and Soil Pollution*, *130*(1), 649–654. https://doi.org/10.1023/A:1013804728336

Qiao, Y., Feng, J., Liu, X., Wang, W., Zhang, P., & Zhu, L. (2016). Surface water pH variations and trends in China from 2004 to 2014. *Environmental Monitoring and Assessment*, *188*(7), 443. https://doi.org/10.1007/s10661-016-5454-5

Ramadan, A. E. K. (2004). *Acid Deposition Phenomena*. 1534.

Rennenberg, H., & Gessler, A. (2001). Acid Rain. In *ELS*. John Wiley & Sons, Ltd. https://doi.org/10.1038/npg.els.0001316

Roshydromet. (2020). *Report on climate features on the territory of the Russian Federation in 2019.* http://www.igce.ru/performance/publishing/reports/

Sase, H., Matsuda, K., Visaratana, T., Garivait, H., Yamashita, N., Kietvuttinon, B., Hongthong, B., Luangjame, J., Khummongkol, P., Shindo, J., Endo, T., Sato, K., Uchiyama, S., Miyazawa, M., Nakata, M., & Lenggoro, I. W. (2012). Deposition Process of Sulfate and Elemental Carbon in Japanese and Thai Forests. *Asian Journal of Atmospheric Environment*, *6*(4), 246–258. https://doi.org/10.5572/ajae.2012.6.4.246

Sase, H., Saito, T., Takahashi, M., Morohashi, M., Yamashita, N., Inomata, Y., Ohizumi, T., & Nakata, M. (2021). Transboundary air pollution reduction rapidly reflected in stream water chemistry in forested catchment on the sea of Japan coast in central Japan. *Atmospheric Environment*, *248*, 118223. https://doi.org/10.1016/j.atmosenv.2021.118223

Sase, H., Takahashi, A., Sato, M., Kobayashi, H., Nakata, M., & Totsuka, T. (2008). Seasonal variation in the atmospheric deposition of inorganic constituents and canopy interactions in a Japanese cedar forest. *Environmental Pollution*, *152*(1), 1–10. https://doi.org/10.1016/j.envpol.2007.06.023

Sase, H., Takahashi, M., Matsuda, K., Sato, K., Tanikawa, T., Yamashita, N., Ohizumi, T., Ishida, T., Kamisako, M., Kobayashi, R., Uchiyama, S., Saito, T., Morohashi, M., Fukuhara, H., Kaneko, S., Inoue, T., Yamada, T., Takenaka, C., Tayasu, I., … Ohta, S. (2019). Response of river water chemistry to changing atmospheric environment and sulfur dynamics in a forested catchment in central Japan. *Biogeochemistry*, *142*(3), 357–374. https://doi.org/10.1007/s10533-019-00540-1

Sase, H., Takahashi, M., Matsuda, K., Yamashita, N., Tsunogai, U., Nakagawa, F., Morohashi, M., Yotsuyanagi, H., Ohizumi, T., Sato, K., Kurokawa, J., & Nakata, M. (2022). Nitrogen saturation of forested catchments in central Japan—Progress or recovery? *Soil Science and Plant Nutrition*, *68*(1), 5–14. https://doi.org/10.1080/00380768.2021.1991228

Sase, H., Yamashita, N., Luangjame, J., Garivait, H., Kietvuttinon, B., Visaratana, T., Kamisako, M., Kobayashi, R., Ohta, S., Shindo, J., Hayashi, K., Toda, H., &

Matsuda, K. (2017). Alkalinization and acidification of stream water with changes in atmospheric deposition in a tropical dry evergreen forest of northeastern Thailand: Alkalinization and acidification of stream water in a tropical forest. *Hydrological Processes*, *31*(4), 836–846. https://doi.org/10.1002/hyp.11062

Schmitz, A., Sanders, T. G. M., Bolte, A., Bussotti, F., Dirnböck, T., Johnson, J., Peñuelas, J., Pollastrini, M., Prescher, A.-K., Sardans, J., Verstraeten, A., & de Vries, W. (2019). Responses of forest ecosystems in Europe to decreasing nitrogen deposition. *Environmental Pollution*, *244*, 980–994. https://doi.org/10.1016/j.envpol.2018.09.101

Schöpp, W., Posch, M., Mylona, S., & Johansson, M. (2003). Long-term development of acid deposition (1880–2030) in sensitive freshwater regions in Europe. *Hydrology and Earth System Sciences*, *7*(4), 436–446. https://doi.org/10.5194/hess-7-436-2003

Shao, S., Burns, D. A., Shen, H., Chen, Y., Russell, A. G., & Driscoll, C. T. (2021). The response of streams in the Adirondack region of New York to projected changes in sulfur and nitrogen deposition under changing climate. *Science of The Total Environment*, *800*, 149626. https://doi.org/10.1016/j.scitotenv.2021.149626

Shimpo, A., Takemura, K., Wakamatsu, S., Togawa, H., Mochizuki, Y., Takekawa, M., Tanaka, S., Yamashita, K., Maeda, S., Kurora, R., Murai, H., Kitabatake, N., Tsuguti, H., Mukougawa, H., Iwasaki, T., Kawamura, R., Kimoto, M., Takayabu, I., Takayabu, Y. N., … Nakamura, H. (2019). Primary Factors behind the Heavy Rain Event of July 2018 and the Subsequent Heat Wave in Japan. *SOLA*, *15A*(0), 13–18. https://doi.org/10.2151/sola.15A-003

Stoddard, J. L., Jeffries, D. S., Lükewille, A., Clair, T. A., Dillon, P. J., Driscoll, C. T., Forsius, M., Johannessen, M., Kahl, J. S., Kellogg, J. H., Kemp, A., Mannio, J., Monteith, D. T., Murdoch, P. S., Patrick, S., Rebsdorf, A., Skjelkvåle, B. L., Stainton, M. P., Traaen, T., … Wilander, A. (1999). Regional trends in aquatic recovery from acidification in North America and Europe. *Nature*, *401*(6753), 575–578. https://doi.org/10.1038/44114

Suzuki, K. (2003). Chemistry of stream water in a snowy temperate catchment. *Hydrological Processes*, *17*(14), 2795–2810. https://doi.org/10.1002/hyp.1434

Vuorenmaa, J., Augustaitis, A., Beudert, B., Clarke, N., Wit, H. A. de, Dirnböck, T., Frey, J., Forsius, M., Indriksone, I., Kleemola, S., Kobler, J., Krám, P., Lindroos, A.-J., Lundin, L., Ruoho-Airola, T., Ukonmaanaho, L., & Váňa, M. (2017). Long-term sulphate and inorganic nitrogen mass balance budgets in European ICP Integrated Monitoring catchments (1990–2012). *Ecological Indicators*, *76*, 15–29. https://doi.org/10.1016/j.ecolind.2016.12.040

Weyhenmeyer, G. A., Hartmann, J., Hessen, D. O., Kopáček, J., Hejzlar, J., Jacquet, S., Hamilton, S. K., Verburg, P., Leach, T. H., Schmid, M., Flaim, G., Nõges, T., Nõges, P., Wentzky, V. C., Rogora, M., Rusak, J. A., Kosten, S., Paterson, A. M., Teubner, K., … Zechmeister, T. (2019). Widespread diminishing anthropogenic effects on calcium in freshwaters. *Scientific Reports*, *9*(1), 10450. https://doi.org/10.1038/s41598-019-46838-w

Yamada, T., Inoue, T., Fukuhara, H., Nakahara, O., Izuta, T., Suda, R., Takahashi, M., Sase, H., Takahashi, A., Kobayashi, H., Ohizumi, T., & Hakamata, T. (2007). Long-term Trends in Surface Water Quality of Five Lakes in Japan. *Water, Air,*

& Soil Pollution: Focus, *7*(1–3), 259–266. https://doi.org/10.1007/s11267-006-9076-8

Yamashita, N., Sase, H., Kobayashi, R., Leong, K.-P., Hanapi, J. M., Uchiyama, S., Urban, S., Toh, Y. Y., Muhamad, M., Gidiman, J., & Chappell, N. A. (2014). Atmospheric deposition versus rock weathering in the control of streamwater chemistry in a tropical rain-forest catchment in Malaysian Borneo. *Journal of Tropical Ecology*, *30*(5), 481–492. https://doi.org/10.1017/S0266467414000303

Yang, R., & Chiwa, M. (2021). Low nitrogen retention in a Japanese cedar plantation in a suburban area, western Japan. *Scientific Reports*, *11*(1), 5335. https://doi.org/10.1038/s41598-021-84753-1

Zhigacheva, E. S., Sase, H., Nakata, M., Ohizumi, T., Gromov, S. A., & Takahashi, M. (2022). Stream water acidification in the Far East of Russia under changing atmospheric deposition and precipitation patterns. *Limnology*. https://doi.org/10.1007/s10201-022-00696-0

Acknowledgements

I would like to thank a number of people for their help and support during the three years of my PhD study.

I would like to express my sincere gratitude to my advisors, Dr. Hiroyuki Sase, Dr. Tsuyoshi Ohizumi, and Prof. Makoto Nakata, for their guiding, constructive feedbacks, kind support, and counseling.

I am extremely grateful to the members of examination committee Dr. Andrew Whitaker and Prof. Shiro Matsuoka for agreeing to be on my thesis committee and providing valuable remarks and comments to the thesis.

Special thanks to all the officers, experts, and scientists in Asia Center for Air Pollution Research (ACAP) for the provided help and a moral support.

I am also grateful to the staff of Institute of Global Climate and Ecology (IGCE), Russia, and especially Dr. Sergey A. Gromov for the help in data retrieval, encouragement and all the support they provided.

I would like to mention all the relevant officers, scientists, and experts from Primorskaya site and Primorsky Center for Environmental Monitoring (PCEM), Russia, for their continuous contribution to sampling, chemical analysis, and quality control of the data.

This study would not have been possible without the financial support by the Higher Agricultural Specialist Program for the Russian Federation Far East at Niigata University, supported by the Ministry of Education, Culture, Sports, Science and Technology (MEXT), Japan.

Additionally, The data at IJR and KJK were collected as the national/EANET monitoring activities in Japan and as one of the Network Center's research activities for the EANET, respectively. Part of the study was supported by the grant from the JSPS KAKENHI Grant Number JP19H00955.